JOURNAL OF PETROLOGY | VOLUME 46 | NUMBER 12 | PAGES 2395–2426 | 2005 | doi:10.1093/petrology/egi057

Evolution of the Magma Chamber beneath Usu Volcano since 1663: a Natural Laboratory for Observing Changing Phenocryst Compositions and Textures

AKIHIKO TOMIYA[1]* AND EIICHI TAKAHASHI[2]

[1]INSTITUTE OF GEOLOGY AND GEOINFORMATION, GEOLOGICAL SURVEY OF JAPAN, AIST, TSUKUBA CENTRAL 7, 1-1-1 HIGASHI, TSUKUBA, IBARAKI, 305-8567, JAPAN

[2]DEPARTMENT OF EARTH AND PLANETARY SCIENCES, TOKYO INSTITUTE OF TECHNOLOGY, 2-12-1 OOKAYAMA, MEGURO-KU, TOKYO, 152-0033, JAPAN

RECEIVED MARCH 23, 2004; ACCEPTED MAY 23, 2005
ADVANCE ACCESS PUBLICATION JULY 8, 2005

We have investigated the evolution of an active silicic magma-feeding system beneath Usu volcano, Japan, where eight eruptions have been recorded since AD *1663. All magmatic products contain similar types of plagioclase and orthopyroxene phenocrysts that consist of homogeneous cores with uniform compositions, and a zoned mantle that increases in size with time. The compositions of plagioclase and orthopyroxene phenocrysts vary gradually and regularly with time, as do the bulk-rock compositions. The texture of these phenocrysts also changes systematically, caused by progressive crystal growth, dissolution and diffusion. On the basis of these observations, we conclude that the same magma-feeding system has persisted at Usu volcano since* AD *1663. Compositional variation of magnetite phenocrysts differs from that of plagioclase and orthopyroxene, because magnetite has large diffusion coefficients and should represent magmatic conditions immediately before the eruption. Most pumices from Usu volcano contain two types of magnetite phenocryst, each with a different composition and crystallization temperature, indicating that two magmas mixed before each eruption (approximately several days before). The end-members changed with time: rhyolite + basaltic andesite (1663); dacite ± rhyolite (1769, 1822, 1853); dacite ± dacite (1977, 2000). The temperature of the magma apparently increases with time, and the increase can be explained by sequential tapping from a magma chamber with a thermal and chemical gradient in addition to injection of high-temperature magma.*

KEY WORDS: *continuous existence of magma chamber; dacite; dissolution and diffusion of phenocrysts; magma mixing; magnetite*

INTRODUCTION

It is generally postulated that a long-lived magma chamber exists beneath an active volcano that repeatedly erupts over relatively short time spans. In such a system, temporal changes in magma composition are common (e.g. Kilauea volcano; Pietruszka & Garcia, 1999) and interpreted as being a result of progressive injection of new magma, fractional crystallization, or crustal assimilation (e.g. DePaolo, 1981; Tomiya & Takahashi, 1995; Feeley & Dungan, 1996; Clynne, 1999). The continuous existence of the same magma chamber is very difficult to prove, however. At some volcanoes, there are suggestions of short-lived magma chambers that experience repeated solidification and remelting (e.g. Koyaguchi & Kaneko, 1999). If the existence of a long-lived magma chamber is verified, it is important to study temporal variations in its characteristics (temperature, oxygen fugacity, volume, injection of new magma, etc.) to make reasonable predictions about future volcanic eruptions.

Research on such problems requires systematic petrological and petrographic analysis of a series of eruptive products for an active volcano that repeatedly erupts within a relatively short time span. Analysis of zoning profiles of phenocrysts is especially effective to constrain the temporal evolution of the magma-feeding system. Many studies of zoning profiles in phenocrysts are restricted to one eruptive product or a series of products in one eruptive episode (e.g. Umino & Horio, 1998; Izbekov

*Corresponding author. Telephone: +81-29-861-3727. Fax: +81-29-856-8725. E-mail: a.tomiya@aist.go.jp

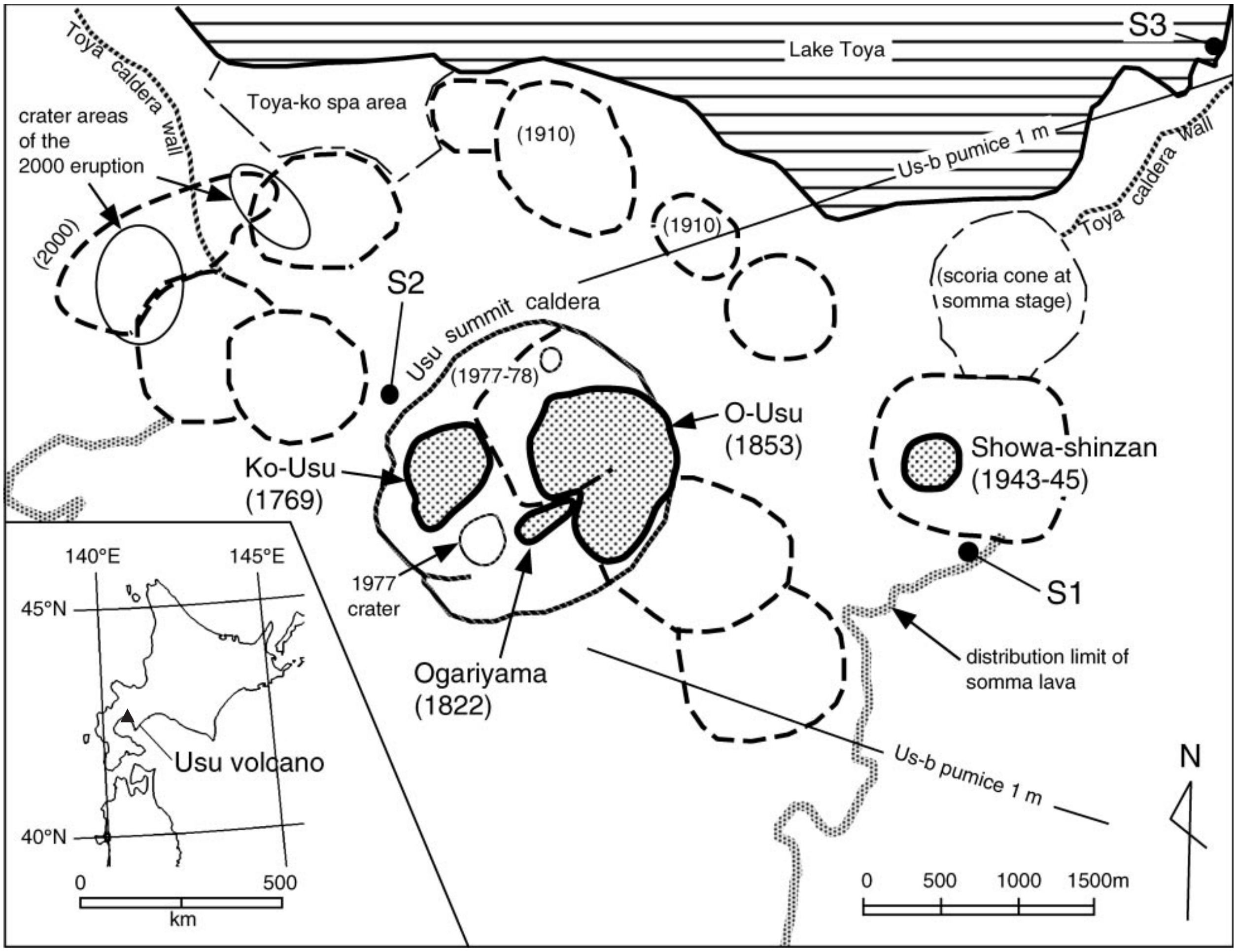

Fig. 1. Outline map of Usu volcano, Japan, indicating the locality of the historical eruption centers and the 1 m isopach of the Us-b pumice, the most voluminous eruptive product in the volcano (after Soya *et al.*, 1981). Usu volcano consists of a main stratocone (e.g. somma lava) with a summit caldera and four lava domes (bold continuous lines) and many cryptodomes (bold dashed lines). Sampling localities (S1, S2, S3 for pumice) are also shown.

et al., 2002; Nakagawa *et al.*, 2002*c*). This is probably because the time span of eruptions is generally too long to link and compare the eruptive products (zoning profiles) with each other, especially for silicic-magma systems. For example, Zellmer *et al.* (2003) studied several products from Montserrat and revealed that the residence times of the phenocrysts are relatively short ($\sim$10 to $\sim$1200 years), and that the time span between each eruption was longer than the residence time.

To make a systematic petrographic study of a silicic system, we selected Usu volcano, Japan (Fig. 1), as a case study. There have been eight recorded eruptions of Usu volcano since AD 1663 within a relatively short time span (of the order of decades; Table 1); thus the petrological relationships between the series of eruptive products can be well resolved. The AD 1663 eruption was the first silicic eruption of Usu volcano after several thousands of years of repose; this eruption separates the recent silicic activity from earlier mafic activity. This eruptive sequence provides an opportunity to construct a magma chamber model for the volcano since AD 1663. Based on a petrological study of the products of the first two eruptions (AD 1663 and 1769), we previously discussed the continuity of the Usu magma chamber and proposed a model for its evolution (Tomiya & Takahashi, 1995). In this paper, the petrological study is extended to all the historical eruption products.

The main observations in this study are the temporal change in the zoning patterns and compositional variation of the phenocrysts. The major components of plagioclase (NaSi–CaAl) and orthopyroxene (Fe–Mg) have small diffusion coefficients (e.g. Ganguly & Tazzoli, 1994; Schwandt *et al.*, 1998; LaTourrette & Wasserburg, 1998); thus, they record the conditions of the magma at the time of crystallization during the past 300 years, since

Table 1: Historical eruptions of Usu volcano

Age (AD)	Precursory seismicity	Vent	Major activity and representative eruptive products	Tephra volume (km^3)
1663	3 days	summit	Plinian (Us-b pumice); pyroclastic surge	2·5
1769*	yes†	summit	sub-Plinian (Us-Va pumice); pyroclastic flow; lava dome (Ko-Usu‡)	0·11
1822	3 days	summit	sub-Plinian (Us-IVa pumice); pyroclastic flow; lava dome (Ogari-yama)	0·28
1853	10 days	summit	sub-Plinian (Us-IIIa pumice); pyroclastic flow; lava dome (O-Usu)	0·35
1910	4·8 days§	N flank	phreatic (no essential material); cryptodome	0·003
1943–1945	6 months	E flank	phreatic–phreatomagmatic; lava dome (Showa-Shinzan)	0·001
1977–1978	1·3 days	summit	sub-Plinian (Us-1977 pumice); phreatic–phreatomagmatic; cryptodome	0·09
2000	4 days	NW flank	phreatomagmatic (Us-2000pm pumice); phreatic; cryptodome	0·001

Data are from Katsui *et al*. (1981), Soya *et al*. (1981) and others.
*There could be an unrecorded tiny eruption prior to the 1769 eruption (Nakagawa *et al*., 2002*b*).
†The duration is unknown.
‡May have formed in 1663.
§Based on a recent revision (Seino *et al*., 2000).

1663. On the other hand, magnetite has large diffusion coefficients, and we hence focus on its core composition, which represents the magmatic conditions just before the eruption. The diffusion coefficient of Ti in magnetite is (1·3–10·3) $\times$ 10^{-17} m^2/s at 800–900°C (Freer & Hauptman, 1978), so the homogenization time for a spherical grain with a radius of 100 μm, for example, is estimated to be about 1·5–12 years, using a solution for diffusion in a spherical solid (e.g. Crank, 1975, p. 92). This time is much shorter than the span between the eruptions of Usu volcano.

In this paper, the continuous existence of the magma chamber since 1663 is demonstrated by comparison of zoning profiles and textures of phenocrysts among the eruptive products. This study is probably the first case where zoning profiles of many eruptive products are successfully compared and the continuous existence of the magma chamber is demonstrated.

USU VOLCANO (GEOLOGICAL BACKGROUND)

Volcanic activity

Usu volcano (Fig. 1) is one of the most active volcanoes in Japan. It has erupted repeatedly at intervals of typically several decades since AD 1663 (Soya *et al*., 1981; Table 1). The volcano started its activity around 10–20 ka (Oba, 1966; Nakagawa, 1998) as a post-caldera cone of the Toya caldera (*c*. 100 ka; Okumura & Sangawa, 1984). Its activity is characterized by bimodal mafic (49–54 wt % SiO_2) and silicic (68–74 wt % SiO_2) magmatism (Oba, 1966; Oba *et al*., 1983). During the early phase of activity, mafic magma erupted and formed a stratocone, referred to as the 'Somma'. About 7–8 ka, a large sector collapse occurred, and formed a horseshoe-shaped caldera. After the collapse, the volcano was dormant for thousands of years. In AD 1663, a Plinian eruption of rhyolitic magma suddenly occurred, signaling the beginning of silicic activity. Since 1663, eight eruptions have been recorded, and many lava domes (or cryptodomes) have formed at the volcano (Soya *et al*., 1981; Table 1, Fig. 1).

The eruptions since 1663 are classified into two types: (1) Plinian, which start with a Plinian or sub-Plinian eruption from the summit (1663, 1769, 1822, 1853, 1977–1978); (2) phreatic–phreatomagmatic, which start with a phreatic–phreatomagmatic eruption from the flank (1910, 1943–1945, 2000). Both eruption types are followed by dome formation except for the 1663 eruption. The 1663 eruption was by far the most voluminous (Table 1).

Previous petrological studies of the post AD 1663 silicic magmatism

There have been several petrological studies of the eruptive products of Usu (e.g. Okumura *et al*., 1981; Oba & Katsui, 1983; Oba *et al*., 1983; Oba, 1991; Tomiya & Takahashi, 1995). The silica content of the rocks tends to decrease with time from 74 wt % (AD 1663) to 69 wt % (AD 2000) (Oba *et al*., 1983; Nakagawa *et al*., 2002*a*; Table 2). The phenocryst content is low (1–6%) in the 1663, 1977–1978 and 2000 rocks, and higher (12–14%) in the 1769 to 1943–1945 rocks (Oba & Katsui, 1983; Tomiya *et al*., 2001; Table 2, Fig. 2). The phenocryst assemblage of the rocks is plagioclase (pl), orthopyroxene (opx), and magnetite (mt). Ilmenite (ilm), clinopyroxene (cpx) and pargasitic hornblende (hb) are also found in some rocks.

Table 2: Whole-rock composition, phenocryst assemblage and phenocryst content

Eruption age (AD):	1663	1769	1822	1853	1943–45	1977–1978	2000	1663
Representative product:	Us-b	Us-Va	Us-IVa	Us-IIIa	Showa-Shinzan	Us-1977	Us-2000pm	mafic magma
*Whole-rock composition (wt %)**								
SiO_2	73·92	71·17	70·73	71·01	70·24	69·65	68·89	54·1
TiO_2	0·21	0·29	0·35	0·31	0·42	0·45	0·47	0·9
Al_2O_3	14·47	15·05	15·62	14·73	14·95	15·07	15·25	20·9
Fe_2O_3	2·55	3·72	3·32	4·37	4·05	4·21	4·46	9·3
MnO	0·15	0·14	0·15	0·11	0·16	0·17	0·17	0·2
MgO	0·31	0·70	0·79	0·72	0·86	0·95	1·01	2·7
CaO	2·20	3·12	3·25	3·39	3·67	3·85	4·07	7·9
Na_2O	4·85	4·44	4·57	4·18	4·61	4·59	4·58	3·5
K_2O	1·21	1·16	1·08	1·00	0·91	0·91	0·91	0·3
P_2O_5	0·13	0·20	0·12	0·17	0·14	0·16	0·16	0·3
Phenocryst assemblage†								
pl	o	o	o	o	o	o	o	o
opx	o	o	o	o	o	o	o	o
mt	o	o	o	o	o	o	o	o
ilm	o	tr	tr	tr	—	—	—	—
cpx	tr	tr	tr	—	—	—	—	o
hb	tr	tr	tr	—	—	—	—	—
Phenocryst content (%)‡	0·5–3·0	11·5	12·5–12·9	13·9	13·0	1·6–5·7	3–6	unknown
Rock texture§	(1)	(2)	(2)	(2)	(2)	(3)	(3)	—

*Data are from Oba *et al.* (1983), except for the 20th-century rocks (Nakagawa *et al.*, 2002*a*) and the mafic magma (Tomiya & Takahashi, 1995). All data are averaged within each product and recalculated to 100%-total basis.
†o, common; tr, trace; —, not found.
‡Data are from Oba & Katsui (1983), except for Us-2000pm (Tomiya *et al.*, 2001). The 1822 and 1853 data are from the corresponding dome lava.
§See text for definition.

The pl and opx phenocrysts in the rocks are classified into three types on the basis of their 'core' compositions (Okumura *et al.*, 1981):

type-A pl: with a homogeneous core of *c.* An_{43};
type-B pl: with a homogeneous core of *c.* An_{90};
type-C pl: others;
type-A opx: with a homogeneous core of *c.* $Mg*_{45}$;
type-B opx: with a homogeneous core of *c.* $Mg*_{73}$;
type-C opx: others;

where An is 100Ca/(Ca + Na) and Mg* is 100Mg/(Mg + Fe) in cation units.

Typically, type-A and type-B phenocrysts are large (up to 1–2 mm) and have a large homogeneous core (Fig. 2). In contrast, type-C phenocrysts are microphenocrysts (up to several hundreds of microns), elongated and significantly zoned with no homogeneous core.

In the 1663 eruptive products, type-A phenocrysts with no mantle are dominant, and type-B phenocrysts are minor (A $\gg$ B; Okumura *et al.*, 1981; Oba, 1991; Tomiya & Takahashi, 1995). In contrast, in the eruptive products since 1769, type-C phenocrysts are dominant and type-A and type-B are minor (C $\gg$ A $\gg$ B). The occurrence of type-C phenocrysts corresponds to an abrupt increase in phenocryst contents from 1663 to 1769 (Fig. 2d; Tomiya & Takahashi, 1995). Type-C phenocrysts often form 'crystal clots' (Oba, 1989), which are interpreted to be mafic inclusions.

These petrographic observations are explained as the products of magma mixing (Okumura *et al.*, 1981; Tomiya & Takahashi, 1995; Fig. 2d):

(1) prior to the 1663 eruption, there was a homogeneous silicic magma (SiO_2 ~74 wt %) with type-A phenocrysts and a homogeneous mafic magma (SiO_2 ~54 wt %) with type-B phenocrysts;

(2) the two magmas mixed during the 1663 eruption and formed a hybrid dacitic magma;

(3) type-C phenocrysts were crystallized rapidly during, or just after, the magma mixing, and the 'crystal clots' represent quenched enclaves of the mafic magma.

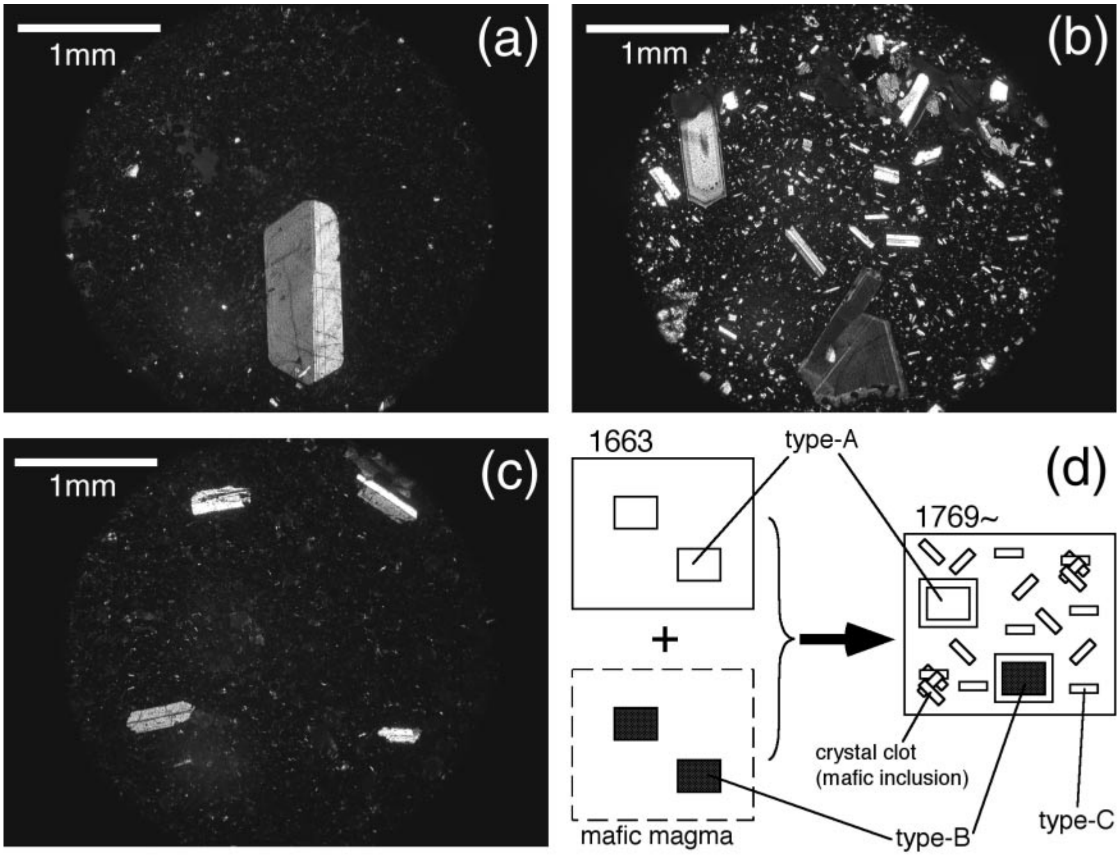

Fig. 2. Three types of texture in the Usu rocks. The photomicrographs were taken with a polarizing microscope using crossed Nicols. (a) Nearly aphyric rock with homogeneous phenocrysts (type-A). Us-b pumice (1663). (b) Porphyritic rock with inhomogeneous phenocrysts. The abundant smaller crystals are type-C microphenocrysts. The larger crystals are type-A or type-B phenocrysts. Us-Va pumice (1769). (c) Nearly aphyric rock with inhomogeneous phenocrysts (mainly type-C). Us-1977 pumice (1977). (d) A schematic sketch of the textural evolution from (a) to (b).

SAMPLING AND ANALYTICAL METHODS

Sampling

To conduct a systematic study of the eruptive products since AD 1663, comprehensive sampling of the eruptive products of Usu volcano (pumice and lava) was carried out. The 1910 eruptive sequence is, however, excluded from this study because it was a phreatic eruption, ejecting only accessory or accidental materials, followed by cryptodome formation.

Most of the studied pumices (1663, 1769, 1822, 1853) were collected at a point on the east flank of the volcano [S1 in Fig. 1; Tomiya & Takahashi (1995, fig. 2)]. The 1977 pumice and the 2000 pumice were collected from the NW (S2 in Fig. 1) and NE flanks (S3 in Fig. 1), respectively. All the pumices are fresh, and white (well vesiculated) to pale gray (less vesiculated) in colour. Samples of the lava domes (1769, 1822, 1853, 1943–1945) were collected from fresh, non-oxidized, parts of each dome.

Sample preparation

Thin sections and polished mounts of the samples were made for observation of their textures and for microprobe analysis of the constituent mineral phases. For the zoning-profile analysis of type-A and type-B phenocrysts, larger phenocrysts were selectively handpicked from crushed samples, mounted in resin, and polished.

For magnetite analysis, we only used pumice samples that were quenched during eruption. Dome lava samples were excluded from the magnetite analysis. Therefore, the 1943–1945 dome rock is excluded from our discussion of magnetite compositions. Hundreds of magnetite crystals were handpicked from each pumice sample, mounted in resin and polished.

Analytical methods

A JEOL JXA-8800M electron microprobe at the Tokyo Institute of Technology and JEOL JXA-8800R and JXA-8900R instruments at the Geological Survey of Japan, AIST, were used for analysis. The analytical conditions

Table 3: Representative compositions of plagioclase, orthopyroxene, clinopyroxene and hornblende phenocrysts

	type-A pl in Us-b*	type-B pl in Us-b	type-C pl in Us-IIIa		type-A opx in Us-b*	type-B opx in Us-b	type-C opx in Us-IIIa	type-A′ opx in Us-1977	cpx in Us-b	hb in Us-b
wt %										
SiO_2	57·45	44·79	53·29	SiO_2	50·40	52·92	52·87	52·77	51·09	44·00
TiO_2	0·01	0·00	0·03	TiO_2	0·09	0·33	0·20	0·00	0·47	2·14
Al_2O_3	26·37	34·40	30·04	Al_2O_3	1·13	2·63	1·19	0·79	3·93	11·43
FeO†	0·17	0·58	0·46	FeO*	32·21	16·08	24·08	26·72	8·55	13·10
MnO	0·01	0·00	0·01	MnO	2·35	0·61	1·40	1·97	0·29	0·53
MgO	0·01	0·06	0·03	MgO	14·09	24·47	20·12	16·03	14·21	13·35
CaO	8·83	18·48	13·27	CaO	0·55	1·29	1·08	0·56	19·93	10·38
Na_2O	6·62	1·05	4·20	Na_2O	0·02	0·00	0·02	0·00	0·36	2·15
K_2O	0·08	0·01	0·05	K_2O	0·00	0·02	0·00	0·00	0·05	0·06
P_2O_5	—	—	—	P_2O_5	—	0·29	—	—	0·34	0·32
Total	99·54	99·37	101·37	Total	100·84	98·63	100·96	98·84	99·22	97·45
An	42·3	90·7	63·4	En	43·3	71·1	58·5	51·0	42·6	—
Ab	57·3	9·3	36·3	Fs	55·5	26·2	39·3	47·7	14·4	—
Or	0·4	0·0	0·3	Wo	1·2	2·7	2·2	1·3	43·0	—
				Mg*	43·8	73·1	59·8	51·7	74·8	64·5

*Average of nine (type-A pl) or eight (type-A opx) analyses.
†Total iron given as FeO.

for quantitative analyses were a 15 kV acceleration voltage and a 12 nA probe current. Counting times for minor elements (Al, Mg, Mn) in magnetite were longer (60–80 s) than others (20–30 s). In the calculation of the ferric/ferrous ratio and ulvöspinel (Usp) component in magnetite, the method of Stormer (1983) was used. The analytical conditions for digital element mapping (Mg and Al distribution in opx) were a 15 kV acceleration voltage and a 20 nA probe current, with a counting time of 1 s per point.

RESULTS

Textural classification

The petrographic texture of the eruptive products changes markedly with time (Fig. 2; Table 2) and can be classified by the abundance and texture of phenocrysts into the following three categories:

(1) nearly aphyric rocks with homogeneous phenocrysts (mainly type-A phenocrysts), such as the 1663 samples (Fig. 2a);

(2) porphyritic rocks with inhomogeneous phenocrysts (mainly type-C microphenocrysts), such as the 1769–1943 samples (Fig. 2b);

(3) nearly aphyric rocks with inhomogeneous phenocrysts (mainly type-C microphenocrysts), such as the 1977 and 2000 samples (Fig. 2c).

All the lava dome rocks (Ko-Usu, Ogari-yama, O-Usu, Showa-Shinzan) are of type (2).

Plagioclase and orthopyroxene phenocrysts

Chemical compositions of the core and rim

Additional plagioclase and orthopyroxene phenocrysts were analyzed, in addition to those of our previous study (Tomiya & Takahashi, 1995). Representative compositions of type-A, B and C phenocrysts are reported in Table 3.

Figure 3 shows the distribution of plagioclase compositions (mol % An) as histograms. The 1663 products show a bimodal distribution (type-A and B), whereas the other products show broad distributions (mainly type-C), as noted by previous workers (Okumura *et al.*, 1981; Oba & Katsui, 1983; Tomiya & Takahashi, 1995). Type-A and type-B plagioclase phenocrysts are found in all products and the total distribution tends to converge around An_{60} towards the 2000 product.

The An content of the rims tends to increase with succeeding eruptions from *c.* An_{43} to An_{58}, as suggested by previous workers, although the trend is not clear in the 1769–1853 samples because of the wide range. In the products of the AD 1663, 1977 and 2000 eruptions, the rim compositions are nearly identical to the mode of the core compositions.

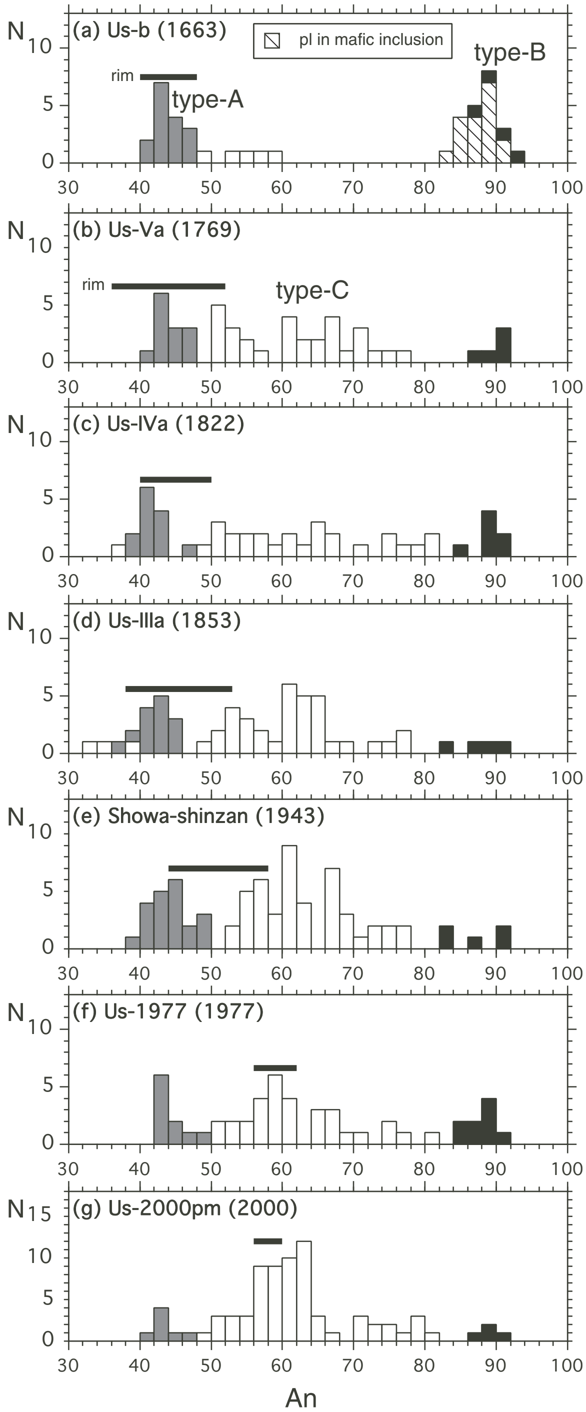

Fig. 3. Histograms of plagioclase composition (core) for each eruptive product. The 1663 product shows a bimodal distribution. The other products show a broad distribution, which tends to converge around An_{60} toward the 2000 product. Type-A (*c.* An_{43}; gray) and type-B (*c.* An_{90}; black) phenocrysts are found in all products, although type-C (white) is dominant, especially in the recent products. The horizontal bar in each histogram represents the range of rim composition. It should be noted that the classification of type-A, -B and -C is based on their texture (e.g. homogeneous core) in addition to their core compositions.

Figure 4 shows the distribution of orthopyroxene compositions as histograms. Again, the bimodal distribution in the 1663 products and the broad distribution in the others is evident. Type-A and type-B opx phenocrysts are also found in almost all products except for those of the 2000 eruption. The distribution of core compositions tends to converge to a narrow compositional range around Mg^*_{63} with time towards the 2000 products. The Mg* of the rims clearly increases with time from *c.* Mg^*_{45} to Mg^*_{63}. Again, the rim composition is nearly identical to the mode of the core composition in the products of the 1663, 1977 and AD 2000 eruptions.

Textures and zoning profiles

BSE (back-scattered electron) images of plagioclase and orthopyroxene are shown in Figs 5–8, and their zoning profiles in Figs 9 and 10. Figures 5 and 9a show the textural and chemical changes in type-A plagioclase with time from 1663 to 2000. In the 1663 product, type-A plagioclase is homogeneous (*c.* An_{43}) and shows a flat zoning profile (Figs 5a and 9a—1663). In the 1769 product, a mantle up to 100 μm in width is formed around a homogeneous core (Figs 5b and 9a—1769). The innermost part of the mantle is typically more sodic (*c.* An_{35}) than the core and we have called it the 'sodic zone' (SZ). There are many small (≤10 μm) melt inclusions aligned along the sodic zone. In the 1822 (Figs 5c and 9a—1822) and 1853 (Figs 5d and 9a—1853) products, the same texture, consisting of a homogeneous core and a mantle with a SZ, is also found. In the plagioclase of the 1943–1945 product (Figs 5e and 9a—1943), a dusty zone (DZ) has developed. Such a dusty texture resembles the products of kinetic experiments in which sodic plagioclase has broken down into calcic plagioclase plus glass (e.g. Tsuchiyama & Takahashi, 1983; Tsuchiyama, 1985; Nakamura & Shimakita, 1998). The DZ is along the innermost part of the mantle, replacing the preexisting SZ (Fig. 11a). In the 1977 and 2000 products (Figs 5f, g, and 9a—1977, 2000), the DZ is larger and infiltrates into the core. The width of mantle of type-A plagioclase tends to become wider with time since 1663. The apparent average growth rate is roughly 0·4–0·7 μm/year.

Figures 7 and 10a show the textural and chemical changes with time of type-A opx. The change of the texture with time is similar to that of plagioclase. In the 1663 product (Figs 7a and 10a—1663), a homogeneous texture and nearly flat zoning profile are observed. In the 1769 product (Figs 7b and 10a—1769), a magnesian mantle with a width of several tens of microns is formed around a more Fe-rich (Mg^*_{45}) core. On the boundary between the core and the mantle, where the Wo (wollastonite) content increases abruptly toward the rim, there are many small (≤10 μm) inclusions of

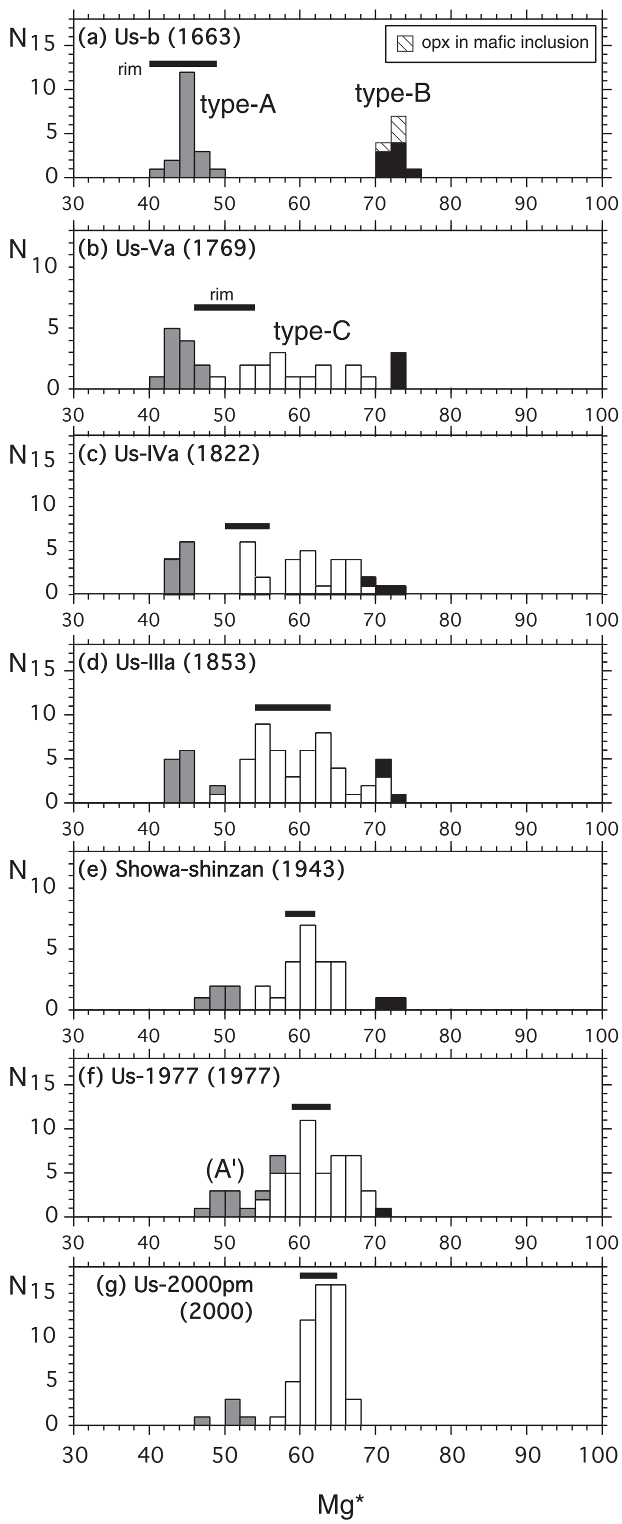

Fig. 4. Histograms of orthopyroxene composition (core) for each eruptive product. Symbols are as in Fig. 3. The distribution pattern is similar to that of plagioclase (Fig. 3). The trend converging toward the 2000 product (Mg^*_{63}) is clearer than that of plagioclase. In the 1977 and 2000 products, there is apparently no type-A (*c.* Mg^*_{45}) in the strict sense; however, a similar type of phenocryst (type-A′) is present.

melt and other minerals (typically magnetite). This mantle texture is similar to that of plagioclase, but the changes in Wo content and Mg* do not correlate with each other; the change in Mg* is gradual and encroaches on the core, which has a homogeneous Wo content (the circle in Fig. 10a—1769). Furthermore, some parts of the core develop an inhomogeneous texture with a more magnesian composition and irregular, large (>20 μm) melt inclusions (Fig. 7b). The same texture is also found in the 1822–1943 products (Figs 7c–e and 10a—1822, 1853, 1943), where the inhomogeneous part with irregular-shaped melt inclusions is enlarged and the homogeneous part of Mg^*_{45} in the core is reduced with time.

In the 1977 product (Figs 7f and 10a—1977), phenocrysts with a homogeneous core of Mg^*_{45} are almost nonexistent. This means that, in the strict sense, there is no type-A opx. However, phenocrysts with similar texture to the type-A opx (large size, irregular-shaped melt inclusions, more ferrous composition than type-C; Fig. 7f) exist. They have the same Wo content (*c.* 1·1–1·5; Fig. 10a—1977; Table 3) as type-A opx. In addition, this type of opx forms a glomeroporphyritic aggregate with type-A pl, similar to type-A opx. Thus, we name this type of opx phenocryst type-A′ and discuss it together with ordinary type-A opx. In the 2000 product (Figs 7g and 10a—2000), type-A′ opx is much less common than in the 1977 samples.

The width of the mantle of type-A opx tends to become wider with time since 1663, although the width of the mantle depends on the crystal's orientation. Along the *a*-axis (e.g. Fig. 10a—1977, 2000), the average growth rate is roughly 0·1–0·2 μm/year. Along the *b*-axis (e.g. Fig. 10a—1769, 1822, 1853, 1943), it is roughly 0·2–0·4 μm/year.

The textures and zoning profiles of type-B pl and opx phenocrysts also change systematically with time in a similar way to those of type-A (type-B pl: Figs 6 and 9b; type-B opx: Figs 8 and 10b). Every type-B phenocryst since 1769 has a mantle whose composition and width are comparable with that of type-A phenocrysts. The growth rates of type-B pl and opx are also comparable with those of type-A pl and opx.

The textures of type-C phenocrysts are variable, as is clear by the definition of type-C; i.e. all phenocrysts except type-A and B ones are classified as type-C. Most of the type-C pl phenocrysts are normally-zoned (Fig. 9c), whereas some are reversely zoned [type-C(R) pl; Fig. 9c—1853C(R)]. Because of the diversity of their textures and compositions, comparison of zoning profiles is generally difficult; however, type-C plagioclase with 'SZ' (Fig. 9c) can be compared with type-A (Fig. 9a) and type-B (Fig. 9b). Their mantles have similar zoning patterns to those of type-A and type-B plagioclase. Type-C(R) pl has a similar zoning profile to the mantle of type-A pl [Fig. 9a—1853, 9c—1853C(R)]; i.e. the core of

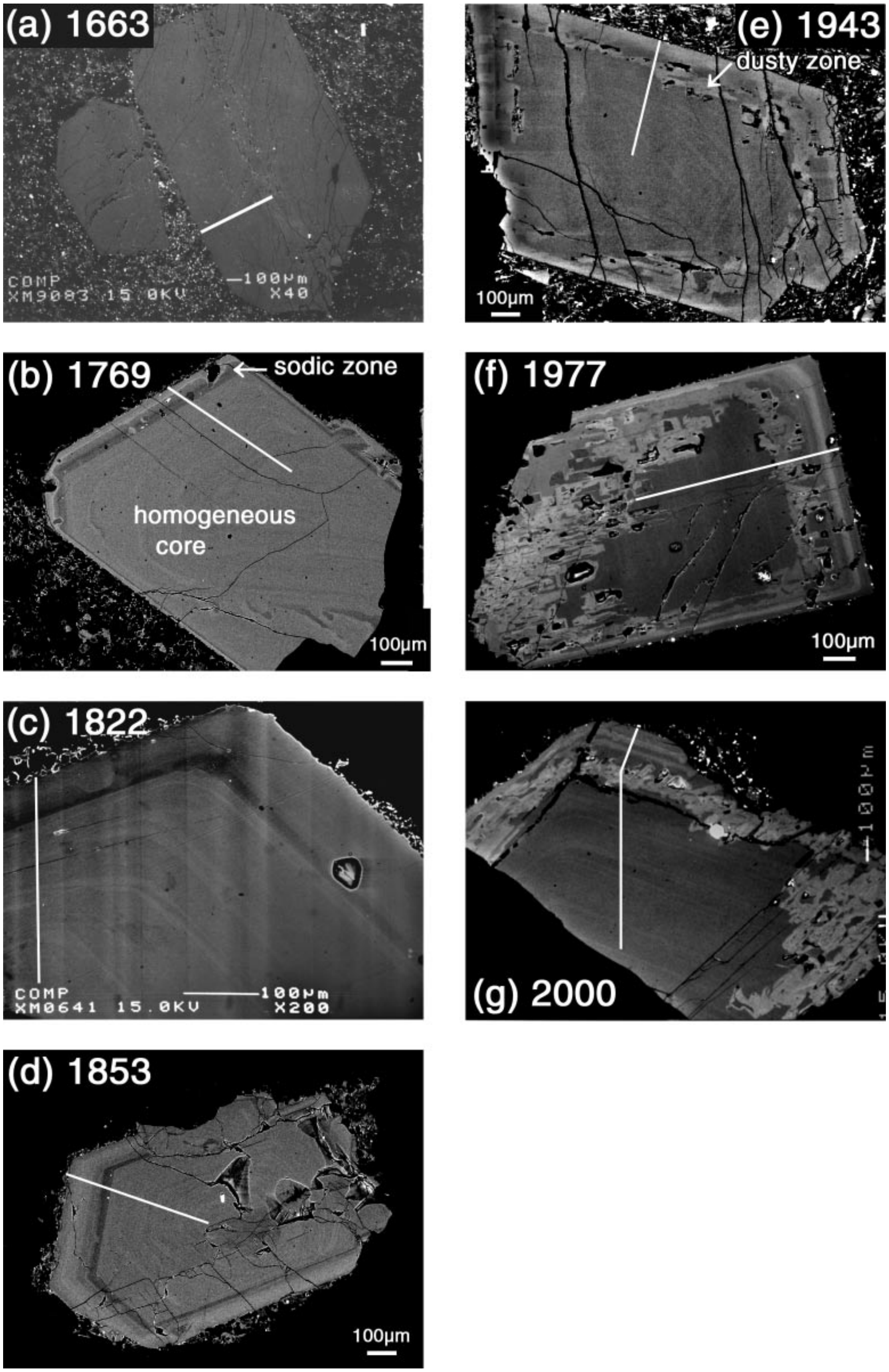

Fig. 5. Texture of the type-A plagioclase phenocrysts as observed in BSE (back-scattered electron) images. There is a large homogeneous core of An_{43}, which has been surrounded by a zoned mantle since 1769. The innermost part of the mantle is a sodic zone (SZ; dark gray band). It should be noted that many small inclusions exist in the SZ. The white lines in the images are the positions of zoning profiles in Fig. 9a. (a) Us-b pumice (1663); (b) Us-Va pumice (1769); (c) Us-IVa pumice (1822); (d) Us-IIIa pumice (1853); (e) Showa-Shinzan lava dome (1943–1945); (f) Us-1977 pumice (1977); (g) Us-2000pm pumice (2000).

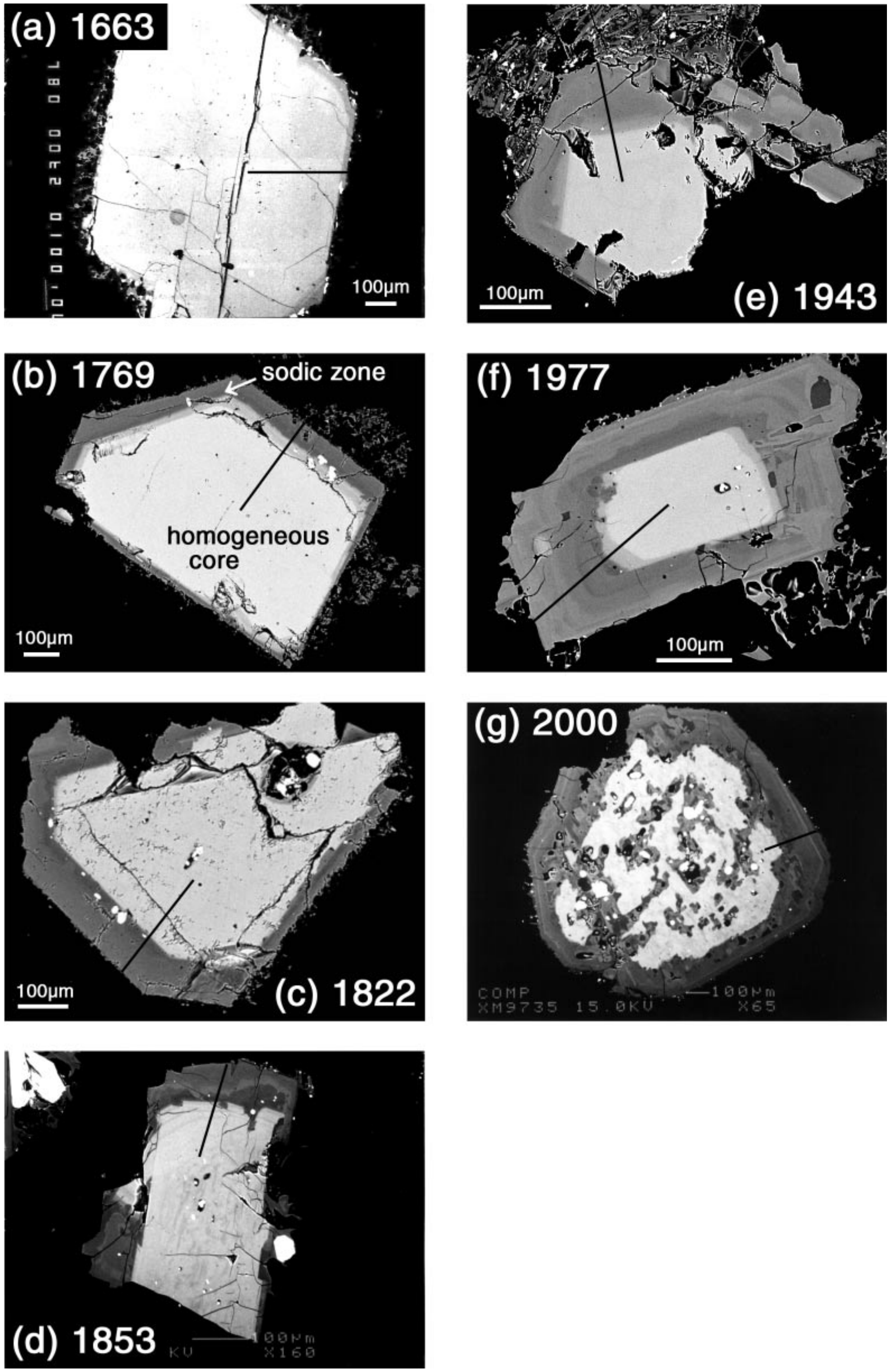

Fig. 6. Texture of the type-B plagioclase phenocrysts as observed in BSE images. A large homogeneous core of An_{90} (bright white area) is surrounded by a zoned mantle since 1769. The innermost part of the mantle is a sodic zone (SZ; dark gray band) as well as type-A. The black lines in the images are the positions of zoning profiles in Fig. 9b. The eruptive products from which the phenocrysts were taken are the same as in Fig. 5.

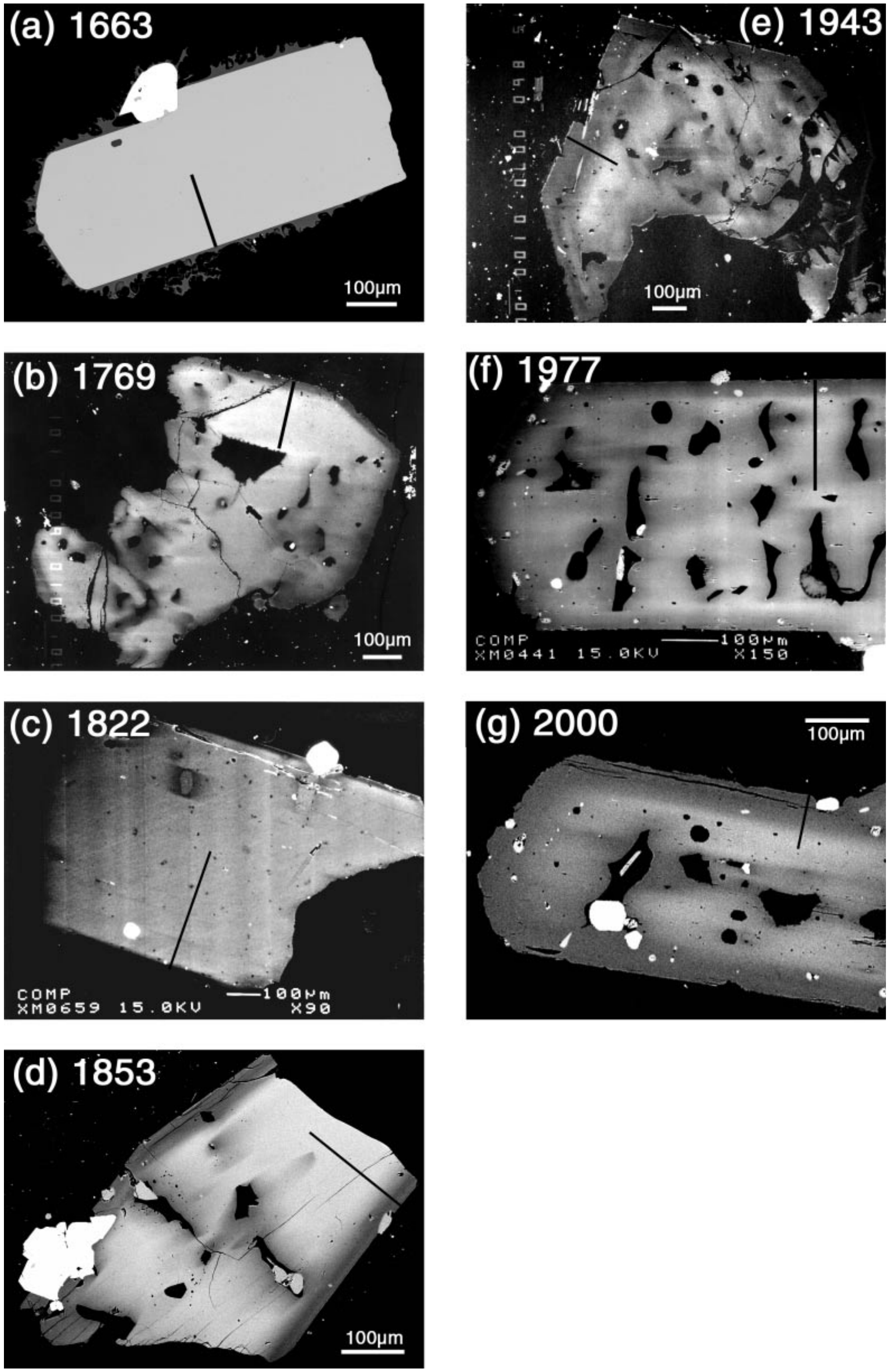

Fig. 7. Texture of the type-A orthopyroxene phenocrysts as observed in BSE images. The homogeneous core (Mg*$_{45}$; bright white area) has been surrounded by a mantle since 1769, and becomes inhomogeneous, developing irregular-shaped melt inclusions (dissolution) and a more magnesian region around them (diffusion). The black lines in the images are the positions of the zoning profiles in Fig. 10a. The eruptive products from which the phenocrysts were taken are the same as in Fig. 5, except for (b), which is from Ko-Usu lava dome.

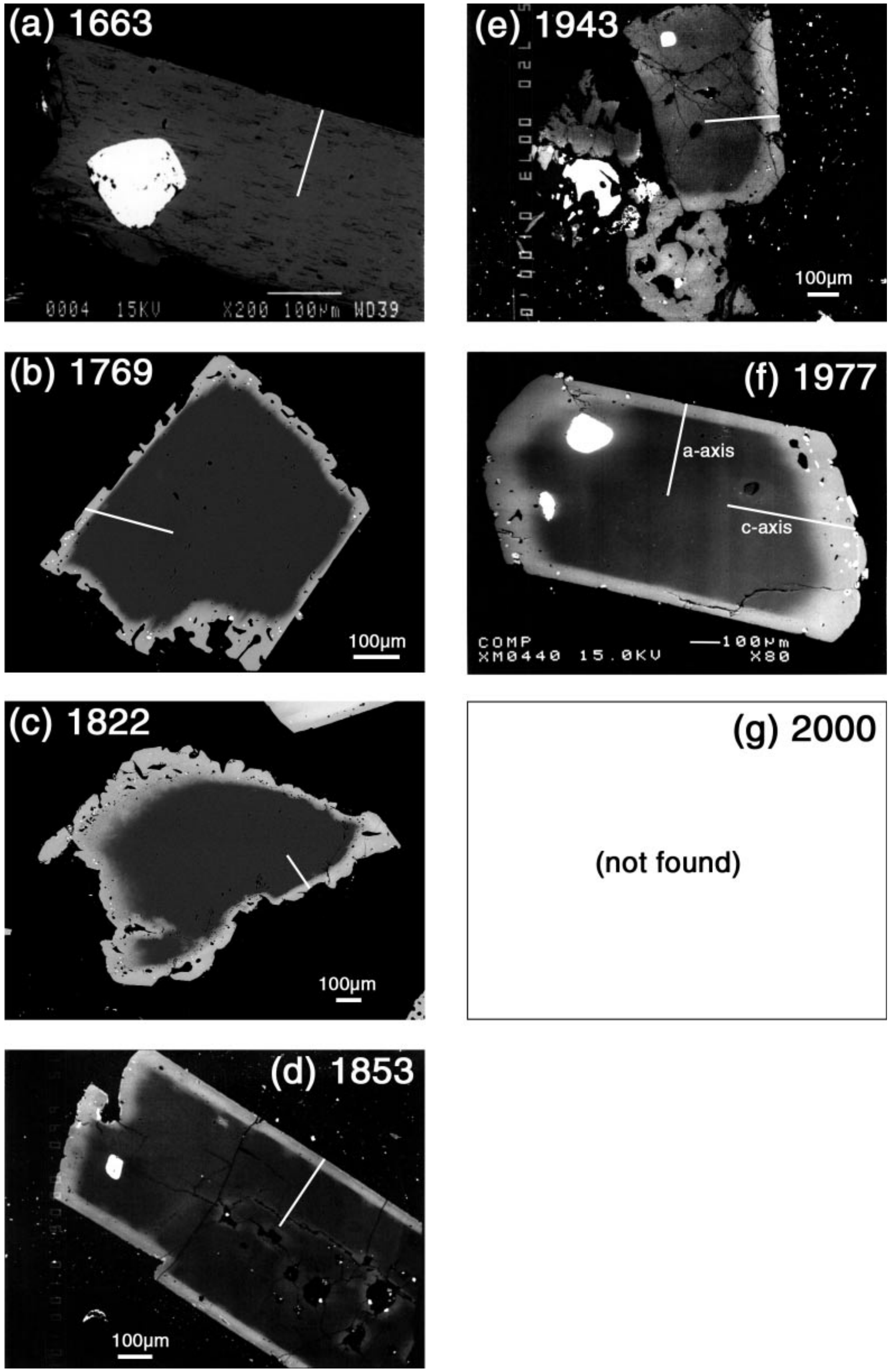

Fig. 8. Texture of the type-B orthopyroxene phenocrysts as observed in BSE images. The homogeneous core (Mg*$_{73}$; dark area) has been surrounded by a mantle since 1769. The sharpness of the boundary between the core and the mantle becomes less because of Fe–Mg interdiffusion, especially along the *c*-axis [elongated direction in (f)]. The white lines in the images are the positions of the zoning profiles in Fig. 10b. The eruptive products from which the phenocrysts were taken are the same as in Fig. 5, except for (d), which is from O-Usu lava dome.

type-C(R) corresponds to SZ. The texture of the type-C opx phenocrysts is more difficult to interpret (Fig. 10c) because there is no appropriate landmark such as SZ in plagioclase. We note, however, that they tend to change to flat profiles (homogeneous) in Mg* with time from normally zoned ones (at 1769). This tendency is consistent with the homogenization of the phenocryst compositions (Fig. 4).

Hornblende and clinopyroxene phenocrysts

Hornblende and clinopyroxene phenocrysts are rarely found in the Usu rocks. In the 1663 eruptive product, they have a homogeneous composition and euhedral texture. The composition of hb is pargasitic and the cpx is magnesian similar to the type-B opx (Table 3). In the 1769 and 1822 products, in contrast, hb and cpx phenocrysts generally have an opacite mantle (Fig. 11b and c). No hb and cpx phenocrysts are found in samples after the 1853 eruption.

Magnetite phenocrysts

Compositions of magnetite and ilmenite

Core compositions are reported as histograms for the following three components: X_{Usp} (Fig. 12a–f; Table 4), Al_2O_3 wt % (Figs 12g–l; 100% recalculated) and Mg/Mn (Fig. 12m–r; cation ratio). The distributions differ from those of plagioclase and orthopyroxene as follows:

(1) magnetite composition is bimodal in the 1822, 1853 and 1977 pumices, as well as the 1663 pumice; however, bimodality in the 1822 and 1853 pumices is not apparent in the major elements (X_{Usp});

(2) magnetite composition is unimodal in the 1769 and 2000 pumices.

In the 1663 pumice, the bimodal distribution of magnetite compositions (Fig. 12a, g, m) is consistent with that of the plagioclase and orthopyroxene (type-A and B; Figs 3a and 4a), with the high-Usp low-Al low-Mg/Mn peak corresponding to type-A, which is dominant in this pumice, and the other corresponding to type-B. In other pumices since the 1769 eruption, however, the peaks of magnetite compositions do not simply correspond to type-A, -B or -C (note that this classification was defined for plagioclase and orthopyroxene).

We have, therefore, made the following classification of the distribution of magnetite compositions other than type-A and -B (Fig. 12; Table 4):

peak-I: the first peak in the histogram (e.g. type-A mt in the 1663 product);

peak-II: the second peak in the histogram, if it exists (e.g. type-B mt in the 1663 product).

Ilmenite is also classified using a similar method to magnetite (Table 4). In the 1663 and 1769 pumice, there is only one peak in ilmenite composition. On the basis of similarity of the Mg/Mn value between magnetite and ilmenite [empirical relation by Bacon & Hirschmann (1988)], the ilmenite is in equilibrium with peak-I mt in each product. In the 1822 and 1853 pumices, there are two peaks in ilmenite composition. Again, using the similarity of Mg/Mn, the two peaks are in equilibrium with peak-I and peak-II mt, respectively (Table 4). This is supported by the observation that magnetite and ilmenite with similar Mg/Mn values are in contact with each other. In the 1977 and 2000 products, no ilmenite is found.

Systematic change of the compositions with time

The composition of each mt peak changes with time (Fig. 12; Table 4). In the pumices erupted since 1769, there is no peak that has the same composition as type-A or type-B in the 1663 pumice, in contrast to plagioclase and orthopyroxene. The Mg/Mn of peak-I mt is the lowest in 1663 (type-A), and increases with time (Fig. 12m–r). The compositions of peak-II mt in the 1822 and 1853 pumices are similar to that in the 1663 pumice (type-A) in Mg/Mn, but they differ in Al_2O_3 content. In contrast to Mg/Mn, the change in Al_2O_3 with time is not as simple (Fig. 12g–l): It decreases from 1663 to 1853 and increases again in 1977 and 2000.

Zoning profiles of magnetite

Figure 13 shows zoning profiles of magnetite phenocrysts (X_{Usp}). Except for the vicinity of the rim (<10–20 μm), the X_{Usp} is homogeneous in each grain. Other compositional parameters, e.g. Mg/Mn and Al_2O_3, are also similarly homogeneous.

Magmatic temperature

Magmatic temperature and oxygen fugacity were determined for the pumices that contain both magnetite and ilmenite (Table 4), based on the Fe–Ti oxide geothermometer of Ghiorso & Sack (1991). The temperature of peak-I increases from 1663 (type-A; *c.* 780°C) to 1853 (*c.* 860°C). The temperatures of peak-II in 1822 and 1853 (*c.* 750°C) are similar to or lower than type-A. The oxygen fugacities (fO_2) of the above pumices plot on a straight line (Fig. 14a). The line is oblique to the NNO (Ni–NiO) and FMQ (fayalite–magnetite–quartz) buffer curves; that is, fO_2 gradually increases, relative to these buffers, with increasing temperature. The temperature for the 1977 and 2000 pumices cannot be estimated from the Fe–Ti oxide geothermometer, because of the lack of ilmenite (Table 4). However, if we assume an empirical relationship between the Mg/Mn of magnetite and temperature (e.g. Oshima, 1977; Bacon & Hirschmann, 1988), the temperature is roughly estimated to be about 900–1000°C.

Neglecting the data from two peak-II ilmenite—magnetite pairs, the temperature increases continuously from 1663 to 2000 (Fig. 14b). This temperature increase correlates with a continuous decrease in silica content in

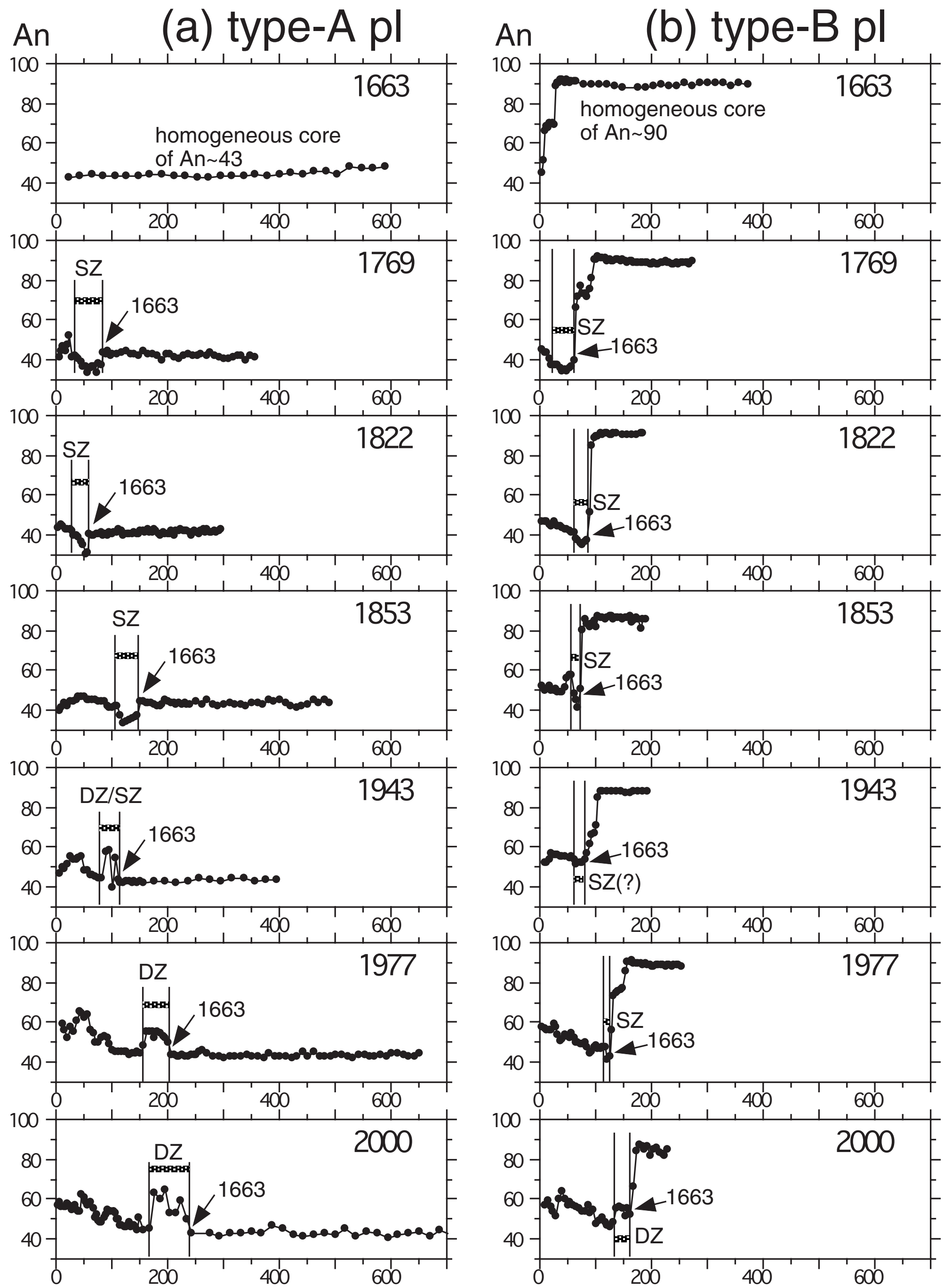

Fig. 9. Zoning profiles (mol % An) of (a) type-A (b) type-B and (c) type-C plagioclase phenocrysts. The homogeneous core and mantle are distinct in type-A and -B pl phenocrysts. The boundary between the core and the SZ (sodic zone) represents the crystal surface in 1663. The abbreviation 'DZ/SZ' means that the SZ is partly changed into DZ (dusty zone). Each analyzed position of the type-A and -B phenocrysts is shown in Figs 5 and 6. The eruptive products from which the type-C phenocrysts were taken are the same as in Fig. 5.

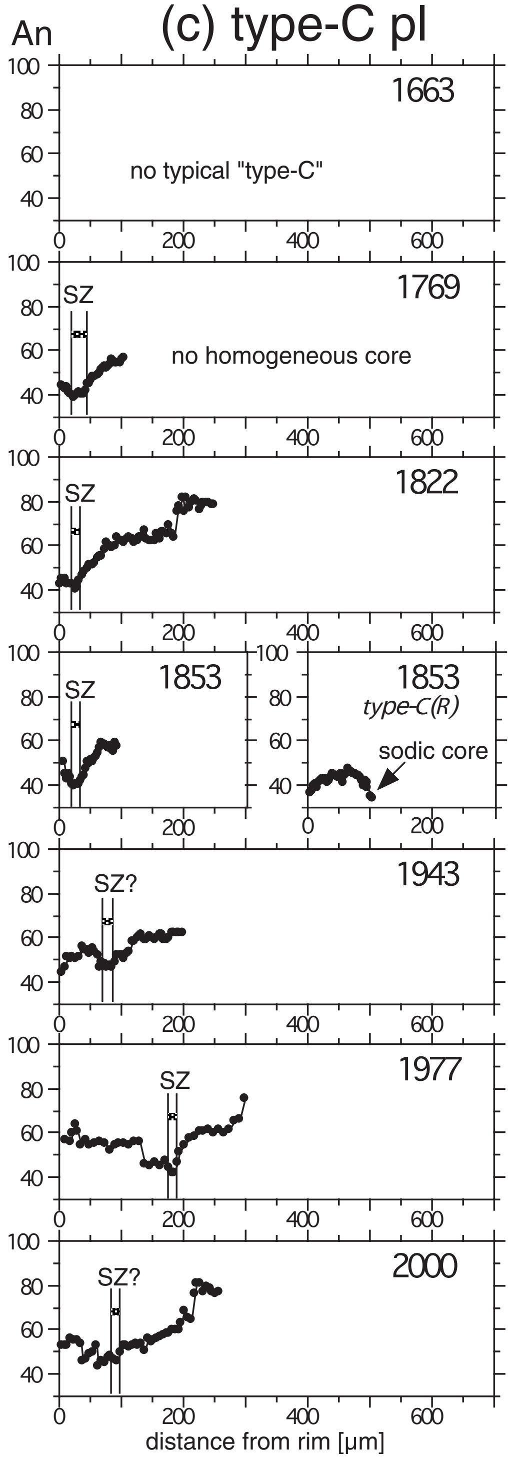

Fig. 9. Continued.

the Usu magma since the 1663 eruption (Fig. 14c; Oba *et al.*, 1983; Nakagawa *et al.*, 2002*a*) and with an increase in the An content of plagioclase (Fig. 3) and Mg* in orthopyroxene (Fig. 4) at the rim.

DISCUSSION

Continuous existence of the magma chamber since the 1663 eruption

Evidence of continuous existence of the magma chamber

As shown previously, type-A and type-B plagioclases always occur in rocks from 1663 to 2000 (Fig. 3), and the pl zoning profiles systematically change with time (Figs 5, 6 and 9). A similar feature is also found in orthopyroxene (Figs 7, 8 and 10), except for the 2000 pumice. In addition, bulk-rock compositions (Fig. 14c) and phenocryst compositions (Figs 3, 4 and 12) systematically change with time. The time span between each eruption is typically several decades. These observations strongly suggest that the magma-feeding system beneath Usu volcano has existed continuously between the 1663 and the 2000 eruption.

Type-A and type-B phenocrysts are inferred to be relics of the silicic magma and the mafic magma, respectively, that mixed during the 1663 eruption. The zoning profiles of these phenocrysts in each succeeding eruption record the change in magmatic conditions during their residence in the magma chamber. Therefore, their mantle corresponds to the record from 1663 to the time of each eruption. On the other hand, type-C phenocrysts are newly formed after 1663. The time when each type-C phenocryst started to crystallize is difficult to determine, causing difficulties in the interpretation of their zoning profiles. Type-C phenocrysts with SZ (Fig. 9c), however, probably existed just after the 1663 eruption because of the similarity of their mantle (SZ and its outside) to type-A and -B phenocrysts. They probably crystallized during the magma-mixing event in 1663, as proposed by Tomiya & Takahashi (1995). Also, type-C(R) started to crystallize at the time of formation of SZ.

Breakdown of plagioclase (formation of dusty zone)

The zoning profiles in plagioclase are caused not only by crystallization but also by dissolution–reaction (Fig. 15). For example, we conclude that the DZ (dusty zone) in plagioclase (Fig. 5e–g) has been formed by dissolution of the SZ (sodic zone) since about 1943. This is based on the observation that the DZ and SZ have appeared together in the same layer of the phenocrysts since 1943, and that the SZ changes gradually into the DZ (Figs 11a and 15a). It should be noted that the DZ does not occur at the rim in contact with the melt, but within the mantle. Thus, the formation of the DZ (i.e. the dissolution of the SZ) is probably caused by an increase in temperature (Fig. 14b). Because dissolution of plagioclase is easiest for the most sodic compositions (e.g. Bowen, 1913), the SZ would be the first part to dissolve during a continuous increase of temperature. The next part to be dissolved would be the core of type-A next to the SZ because of its low An content; this situation is indeed observed in the 1977 and 2000 pumices (Fig. 5f and g).

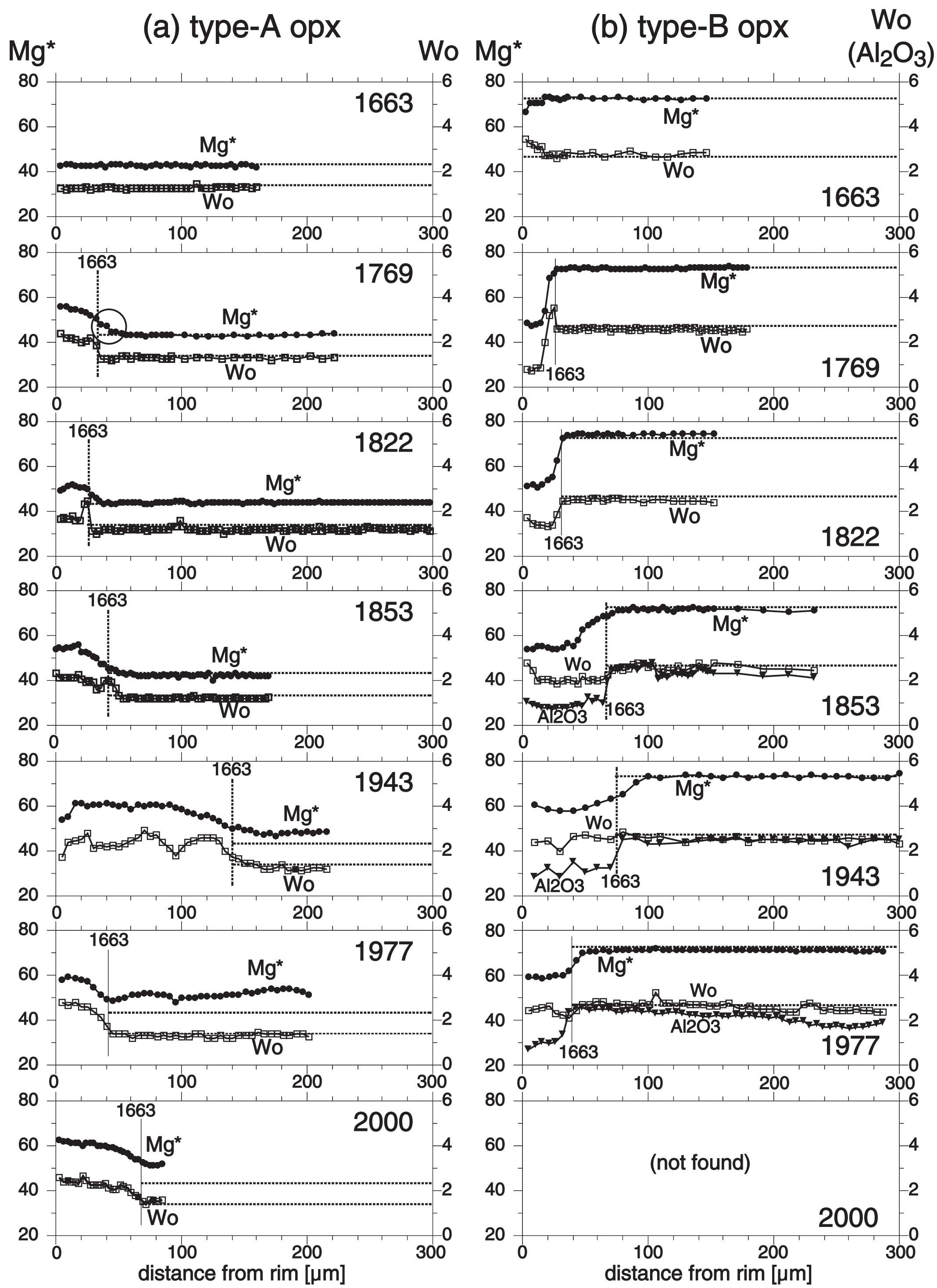

Fig. 10. Zoning profiles [Mg* = 100Mg/(Mg + Fe) and mol % Wo] of (a) type-A, (b) type-B and (c) type-C orthopyroxene phenocrysts. A homogeneous core and distinct mantle are seen in both type-A and -B phenocrysts, as in plagioclase. The boundary between the core and the mantle (i.e. the crystal surface in 1663) can be seen as a gap in Wo (or Al_2O_3) content. The profiles where the 1663 surface is marked with a vertical continuous line are for the *a*-axis, whereas those marked with a vertical dotted line are for the *b*-axis. The *b*-axis profiles represent diffusion patterns; the boundary between the core and mantle is sharp for Wo but gradual for Mg* [e.g. highlighted by the circle in (a)—1769]. The horizontal dotted lines represent the homogeneous core compositions (Mg^*_{43} and $Wo_{1\cdot3}$ for type-A; Mg^*_{73} and $Wo_{2\cdot7}$ for type-B). Each analyzed position of type-A and -B phenocryst is shown in Figs 7 and 8. The eruptive products from which the type-C phenocrysts were taken are the same as in Fig. 5.

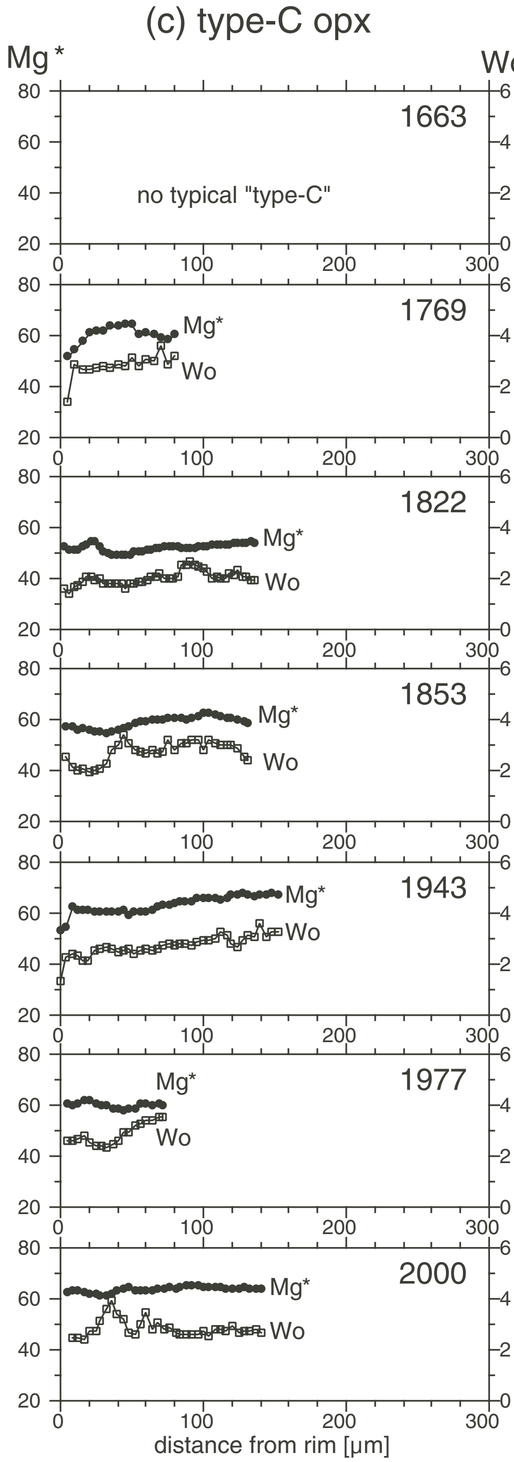

Fig. 10. Continued.

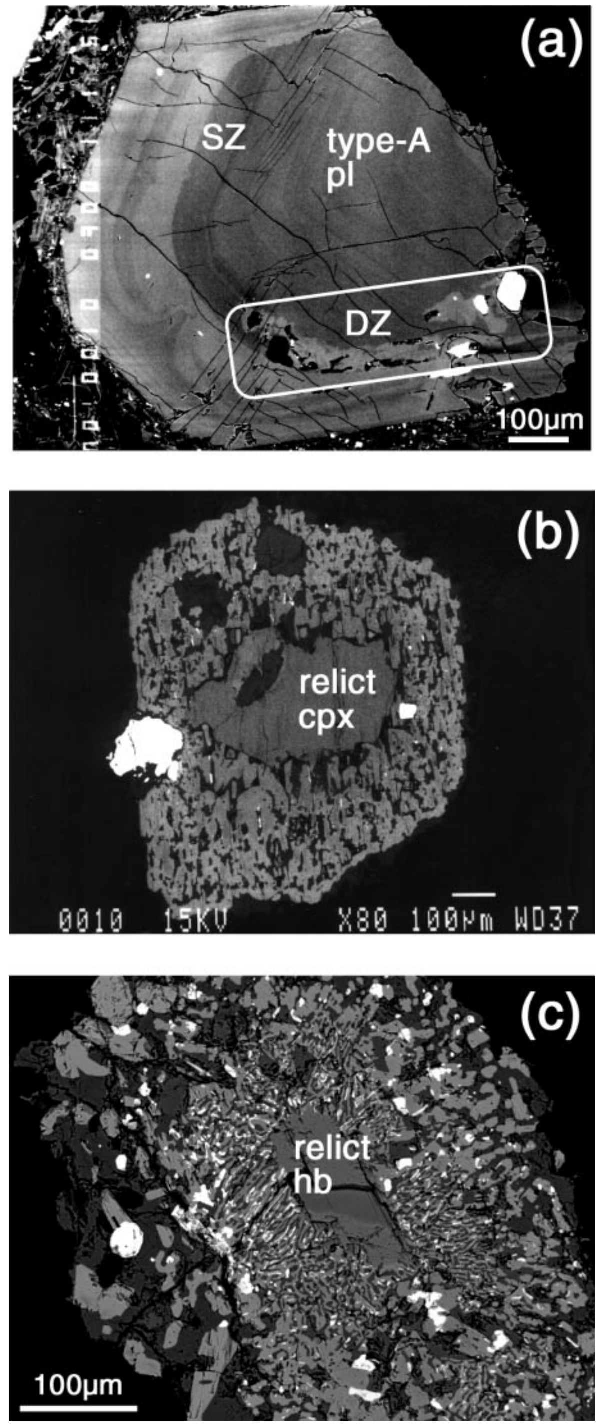

Fig. 11. Dissolution of phenocrysts as observed in BSE images. (a) Dusty zone (DZ) of plagioclase phenocryst in the 1943 product. The DZ is replacing the sodic zone (SZ). (b) Clinopyroxene (cpx) in the 1769 product (Us-Va pumice). The core (denoted as 'relict cpx') has the same composition as type-B cpx in the 1663 product (Mg^*_{73}). The opacite mantle mainly consists of opx (gray) + pl (blackish gray) + glass (black). (c) Hornblende (hb) in the 1822 product (Us-IVa pumice). The core (denoted as 'relict hb') has the same composition as pargasitic hb in the 1663 product (Mg^*_{62} and 12% Al_2O_3). The opacite mantle consists of opx (bright gray) + mt (white) + glass (black).

Interdiffusion between Fe and Mg within orthopyroxene

Interdiffusion between Fe and Mg (and Mn) appears to have occurred within orthopyroxene phenocrysts

(Fig. 15b). For example, the discrepancy between the Mg* and Wo zoning profiles in the 1769 opx (Fig. 10a—1769) can be easily explained by assuming that Fe–Mg interdiffusion took place over about one hundred years (1663–1769), but that Ca diffusion was much slower.

To verify the diffusion hypothesis, we conducted numerical simulation experiments to reproduce both diffusion and growth in a crystal. Details of the simulation are explained in the Appendix; here we present only selected results from this simulation. Figure 16a–f demonstrates the results of a series of calculations, simulating growth and diffusion in a type-A opx phenocryst for about 300 years since 1663. Simulations are shown for different crystal shapes: case 1 (plate) and case 2 (cylinder) (see Appendix). In these calculations, the initial composition C_{core} is $Mg*_{43}$, and the diffusion coefficient D, the growth rate G, and the rim composition C_{rim} are held constant; i.e. $D = 2{\cdot}0 \times 10^{-20}$ m^2/s (Ganguly & Tazzoli, 1994; for b-axis with $T = 850°C$ and $X_{Fe} = 0{\cdot}4$), $G = 0{\cdot}4$ μm/year

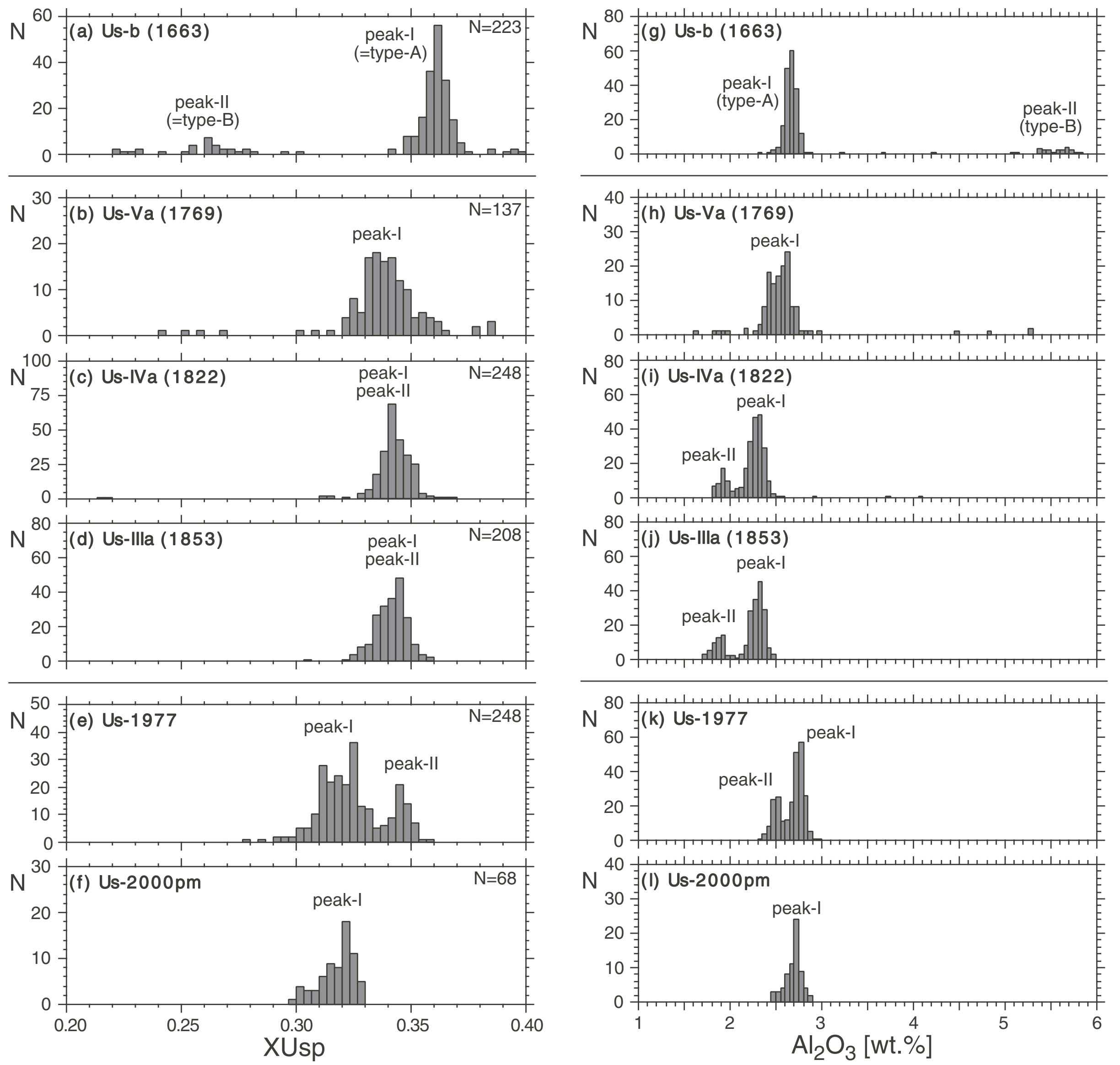

Fig. 12. Histograms of magnetite composition (core) for each pumice. (a)–(f) Usp component (X_{Usp}); (g)–(l) Al_2O_3 content; (m)–(r) Mg/Mn (cation ratio). It should be noted that the right-hand panel of (m) has a different horizontal axis because of the large Mg/Mn of type-B mt. In contrast to pl (Fig. 3) and opx (Fig. 4), bimodality is clear in the 1822, 1853 and 1977 pumices as well as the 1663 pumice. The horizontal lines between 1663 and 1769 and between 1853 and 1977 represent the distinct changes in rock texture (1, 2, 3) (see text for details). The textural change corresponds to the marked change in the histogram.

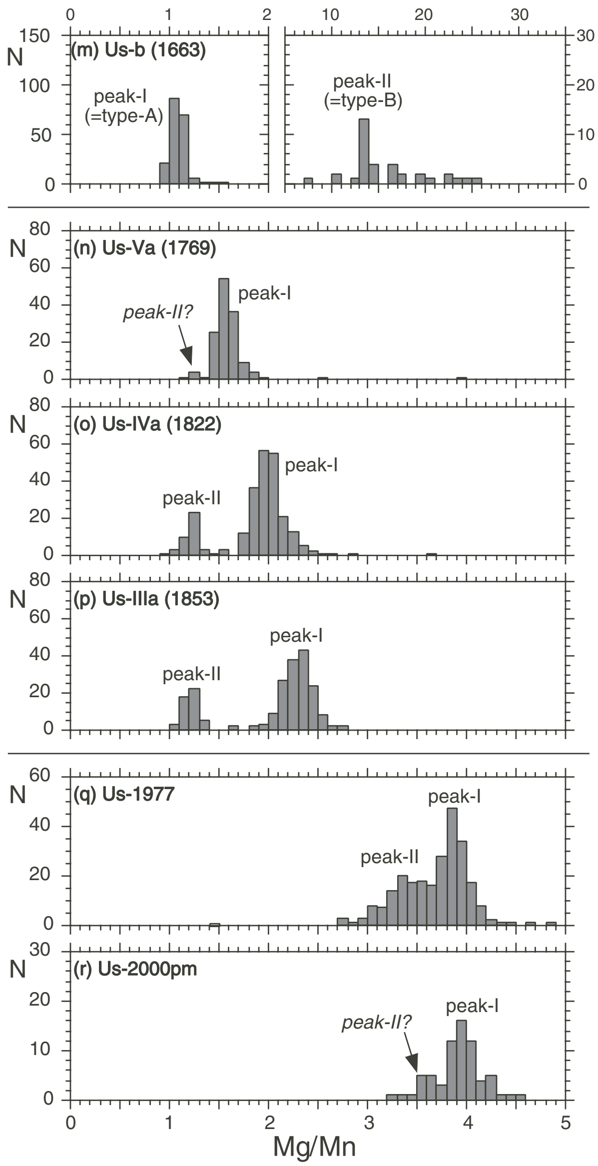

Fig. 12. Continued.

and $C_{rim} = Mg*_{58}$. If we plot the zoning profiles along the *b*-axis (Fig. 10a—1663, 1769, 1822, 1853, 1943), the model results (Fig. 16a–e) and the actual compositions roughly agree. The curvature (the transition from C_{core} to C_{rim}) of the profiles is especially well fitted by the model calculation. The disagreement in growth width (mantle width) is not an important problem because the difference in growth rate (and hence growth width) does not affect the curvature much (Fig. 16g). In addition, even within a single sample, there is variation in mantle width, which is probably caused by variation in individual phenocryst size, distance between phenocrysts, and so on.

A similar numerical simulation was also performed for type-B opx. Figure 16h and i shows examples of fitting for the *a*-axis and *c*-axis in a crystal (Fig. 8f) in the 1977 pumice, respectively. The *a*-axis profile can be fitted by $D = 0{\cdot}11 \times 10^{-20}$ m^2/s, much smaller than the *b*-axis value, whereas that of the *c*-axis can be fitted by the same value as the *b*-axis ($D = 2{\cdot}0 \times 10^{-20}$ m^2/s). This is consistent with the theoretical prediction by Ganguly & Tazzoli (1994) that Fe–Mg interdiffusion is slowest along the *a*-axis.

On the other hand, the zoning profiles of type-A′ opx in the 1977 and 2000 products are difficult to explain only by diffusion. As seen in Fig. 16f, the center of the crystal is not affected by diffusion if its size is 200 μm or greater. This is also the case even if the diffusion coefficient is ten times bigger (e.g. Fig. A2d). This is inconsistent with the observation that no type-A′ opx remains with the original core composition ($Mg*_{45}$). Thus, we must account for the effect of dissolution.

To distinguish between the effects of dissolution and diffusion, we obtained digital map images of type-A (Fig. 17a–d) and type-A′ opx (Fig. 17e and f). In the 1663 pyroxene (Fig. 17a), the Mg concentration is homogeneous. This homogeneous core is significantly reduced in the 1853 pyroxene (Fig. 17c) and disappears in the 1977 pyroxene (Fig. 17e). On the other hand, a high-Mg region is well developed, especially along the *c*-axis (elongated direction), around the irregular-shaped melt inclusions.

The possibility that these high-Mg regions were produced by dissolution–recrystallization processes can be rejected as follows. To distinguish dissolution–recrystallization from Fe–Mg interdiffusion, we use the Al distribution map because Al is virtually unaffected by diffusion over the past 300 years (e.g. Sautter *et al.*, 1988; Smith & Barron, 1991). In the 1663 pyroxene (Fig. 17b), the type-A opx shows sector zoning with low Al content in the *c*-axis direction, and there are streaks. In the 1853 and 1977 pyroxene (Fig. 17d and f), a similar texture (sector zoning and streaks) remains, although dissolution is seen at and around the irregular-shaped melt inclusions. The observation that the streaks (representing the original Al distribution) remain in the high-Mg region is strong evidence that the high-Mg region is produced not by dissolution–recrystallization processes but by Fe–Mg diffusion. The same argument can be made on Ca distribution (Fig. 10a—1977). We therefore conclude that type-A′ opx are converted from type-A opx by Fe–Mg interdiffusion, assisted by dissolution (Fig. 15b).

Breakdown of clinopyroxene and hornblende

Clinopyroxene and hornblende phenocrysts in the 1769 and 1822 products are disequilibrium phases, judging from their opacite mantles (Fig. 11b and c). They are residues of phenocrysts that were derived from the mafic magma (cpx) and from the boundary layer (hb) between

Table 4: Chemical compositions of magnetite and ilmenite in the studied pumices

	Magnetite									
Age (AD):	1663		1769	1822		1853		1977		2000
Pumice:	Us-b		Us-Va	Us-IVa		Us-IIIa		Us-1977		Us-2000pm
	type-A	type-B	peak-I	peak-I	peak-II	peak-I	peak-II	peak-I	peak-II	peak-I
n:	187	36	133	205	41	160	48	176	72	68
wt %										
SiO_2	0·10 ± 0·05	0·12 ± 0·05	0·08 ± 0·05	0·06 ± 0·04	0·06 ± 0·04	0·06 ± 0·04	0·06 ± 0·05	0·08 ± 0·04	0·07 ± 0·04	0·08 ± 0·02
TiO_2	11·92 ± 0·28	8·03 ± 0·96	11·05 ± 0·52	11·33 ± 0·27	11·44 ± 0·11	11·29 ± 0·27	11·38 ± 0·15	10·39 ± 0·30	11·28 ± 0·24	10·43 ± 0·29
Al_2O_3	2·63 ± 0·08	5·84 ± 0·92	2·43 ± 0·18	2·24 ± 0·11	1·87 ± 0·05	2·25 ± 0·08	1·83 ± 0·07	2·67 ± 0·08	2·44 ± 0·06	2·63 ± 0·09
FeOt*	78·15 ± 0·78	76·26 ± 0·94	76·77 ± 0·84	78·09 ± 0·45	78·52 ± 0·43	78·09 ± 0·44	78·67 ± 0·48	77·45 ± 0·74	77·00 ± 0·91	77·39 ± 0·68
MnO	0·97 ± 0·04	0·40 ± 0·10	0·98 ± 0·07	0·89 ± 0·04	0·97 ± 0·04	0·86 ± 0·04	0·98 ± 0·04	0·75 ± 0·03	0·83 ± 0·04	0·76 ± 0·03
MgO	0·61 ± 0·07	3·34 ± 0·31	0·88 ± 0·08	1·02 ± 0·08	0·67 ± 0·04	1·12 ± 0·05	0·68 ± 0·04	1·64 ± 0·05	1·52 ± 0·10	1·70 ± 0·06
Recalculated analyses										
FeO	40·36 ± 0·34	33·74 ± 1·06	38·39 ± 0·62	38·94 ± 0·39	39·41 ± 0·22	38·81 ± 0·33	39·34 ± 0·25	37·20 ± 0·40	38·10 ± 0·41	37·13 ± 0·46
Fe_2O_3	41·99 ± 0·75	47·25 ± 1·13	42·64 ± 0·97	43·50 ± 0·54	43·46 ± 0·38	43·65 ± 0·52	43·70 ± 0·44	44·72 ± 0·77	43·23 ± 0·80	44·73 ± 0·54
Total	98·58 ± 0·79	98·72 ± 0·83	96·46 ± 0·95	97·98 ± 0·54	97·88 ± 0·47	98·05 ± 0·53	97·96 ± 0·59	97·46 ± 0·80	97·47 ± 1·01	97·46 ± 0·87
X_{Usp}	0·362 ± 0·009	0·253 ± 0·030	0·341 ± 0·015	0·342 ± 0·008	0·345 ± 0·004	0·341 ± 0·008	0·342 ± 0·005	0·317 ± 0·009	0·343 ± 0·008	0·318 ± 0·008
Mg/Mn	1·10 ± 0·15	15·55 ± 4·51	1·60 ± 0·25	2·02 ± 0·20	1·21 ± 0·09	2·29 ± 0·16	1·21 ± 0·07	3·85 ± 0·23	3·24 ± 0·28	3·93 ± 0·24

Table 4: continued

	Ilmenite									
Age (AD):	1663		1769	1822		1853		1977		2000
Pumice:	Us-b		Us-Va	Us-IVa		Us-IIIa		Us-1977		Us-2000pm
	type-A	type-B	peak-I	peak-I	peak-II	peak-I	peak-II	peak-I	peak-II	peak-I
n:	5		21	8	1	3	2			
wt %										
SiO_2	0·00 ± 0·01		0·03 ± 0·03	0·04 ± 0·03	0·01	0·02 ± 0·04	0·04 ± 0·01			
TiO_2	47·73 ± 0·28		46·12 ± 0·58	46·93 ± 0·60	48·70	46·53 ± 0·12	48·49 ± 0·92			
Al_2O_3	0·16 ± 0·02		0·17 ± 0·02	0·18 ± 0·02	0·11	0·19 ± 0·01	0·11 ± 0·00			
FeOt*	46·86 ± 0·35	(not exist)	46·98 ± 0·55	48·20 ± 0·28	47·04	48·76 ± 0·11	47·09 ± 0·05	(not exist)	(not exist)	(not exist)
MnO	1·50 ± 0·10		1·46 ± 0·05	1·27 ± 0·05	1·61	1·18 ± 0·03	1·59 ± 0·03			
MgO	1·20 ± 0·07		1·60 ± 0·06	1·73 ± 0·06	1·37	1·97 ± 0·01	1·31 ± 0·02			
Recalculated analyses										
FeO	39·25 ± 0·26		37·17 ± 0·52	37·87 ± 0·58	39·73	37·15 ± 0·10	39·70 ± 0·83			
Fe_2O_3	8·46 ± 0·25		10·90 ± 0·89	11·48 ± 0·89	8·12	12·90 ± 0·10	8·21 ± 0·88			
Total	98·34 ± 0·59		97·44 ± 0·75	99·49 ± 0·35	99·65	99·94 ± 0·18	99·45 ± 0·90			
X_{Ilm}	0·912 ± 0·002		0·883 ± 0·010	0·880 ± 0·010	0·916	0·865 ± 0·001	0·915 ± 0·010			
Mg/Mn	1·41 ± 0·19		1·93 ± 0·10	2·41 ± 0·16	1·50	2·95 ± 0·07	1·45 ± 0·06			
Al_2O_3	0·17 ± 0·02		0·17 ± 0·02	0·18 ± 0·02	0·11	0·19 ± 0·01	0·12 ± 0·00			
T (°C)†	778	1020‡	825	830	748	858	750			
$\log(fO_2)$	−14·9		−13·4	−13·2	−15·7	−12·5	−15·6			

Average and standard deviation of *n* analyses. 'Peak-II?' is incorporated with peak-I in the 1769 and 2000 pumice.
*Raw data.
†Based on the Fe–Ti oxide geothermometer of Ghiorso & Sack (1991) except for type-B in 1663.
‡From pyroxene thermometry (Tomiya & Takahashi, 1995).

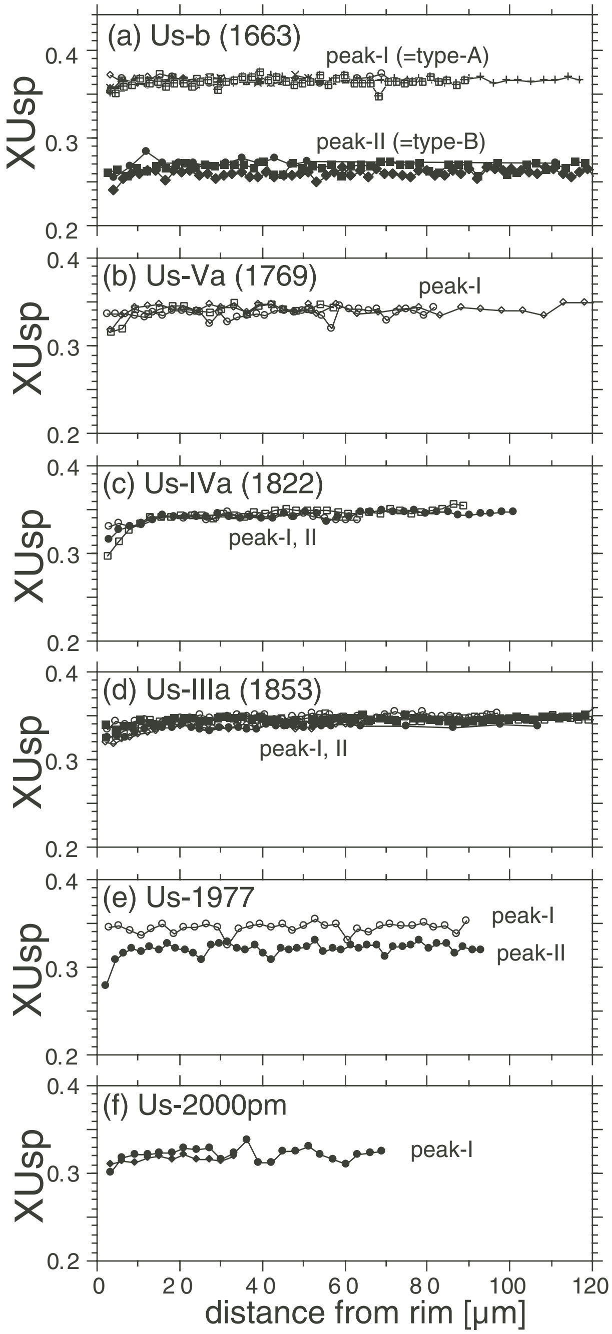

Fig. 13. Zoning profile (X_{Usp}) of magnetite phenocryst in each pumice. The grains are homogeneous except in the vicinity of the rim (<10–20 μm).

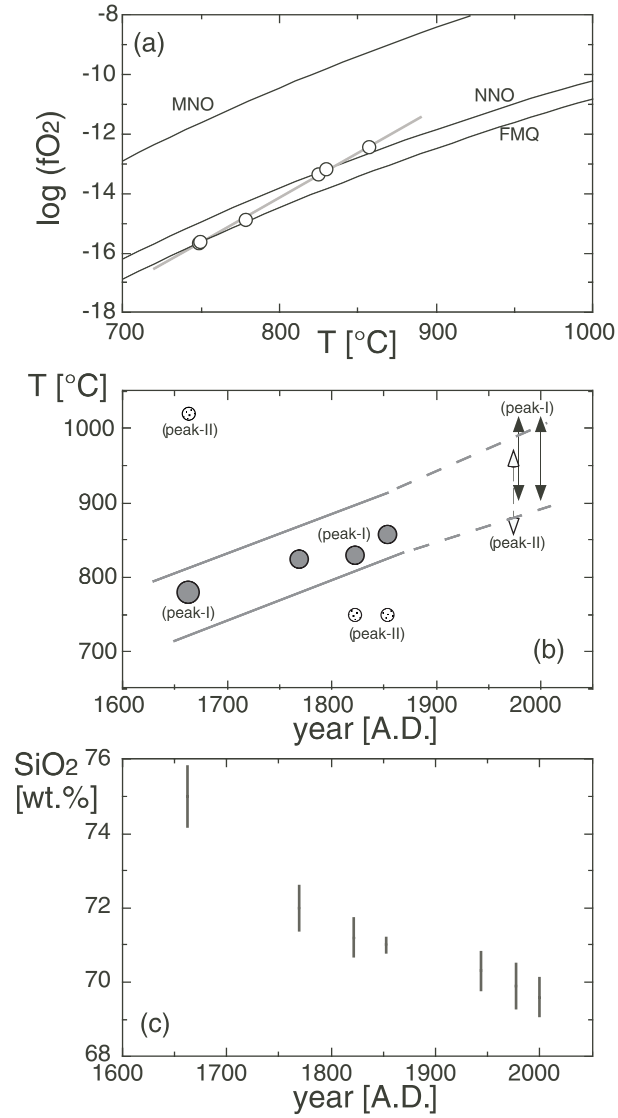

Fig. 14. (a) Magmatic temperature and oxygen fugacity (fO_2) estimated using the Fe–Ti oxide geothermometer of Ghiorso & Sack (1991). The buffer lines (MNO, NNO, FMQ) are based on Chou (1987). (b) Temporal change in magmatic temperature. (c) Temporal change in silica content (Nakagawa *et al.*, 2002*a*). The temperature increase for the magmas represented by peak-I corresponds to the change in magmatic composition (decrease of silica).

the silicic magma and the mafic magma, respectively (Tomiya & Takahashi, 1995). They were homogeneous and euhedral just after the magma mixing event in 1663, but the opacite mantle was gradually formed by dissolution (breaking-down) of the phenocrysts since 1663 (Fig. 15c). The rates of dissolution for cpx and hb were faster than those of type-A pl and opx, because these phases had disappeared by 1853.

Magma mixing prior to each eruption

According to our model, extensive magma mixing occurred in the 1663 eruption (Tomiya & Takahashi, 1995). The existence of type-A and type-B phenocrysts since 1769 (Figs 3 and 4) is evidence of magma mixing in 1663, not just prior to each eruption. Whether or not

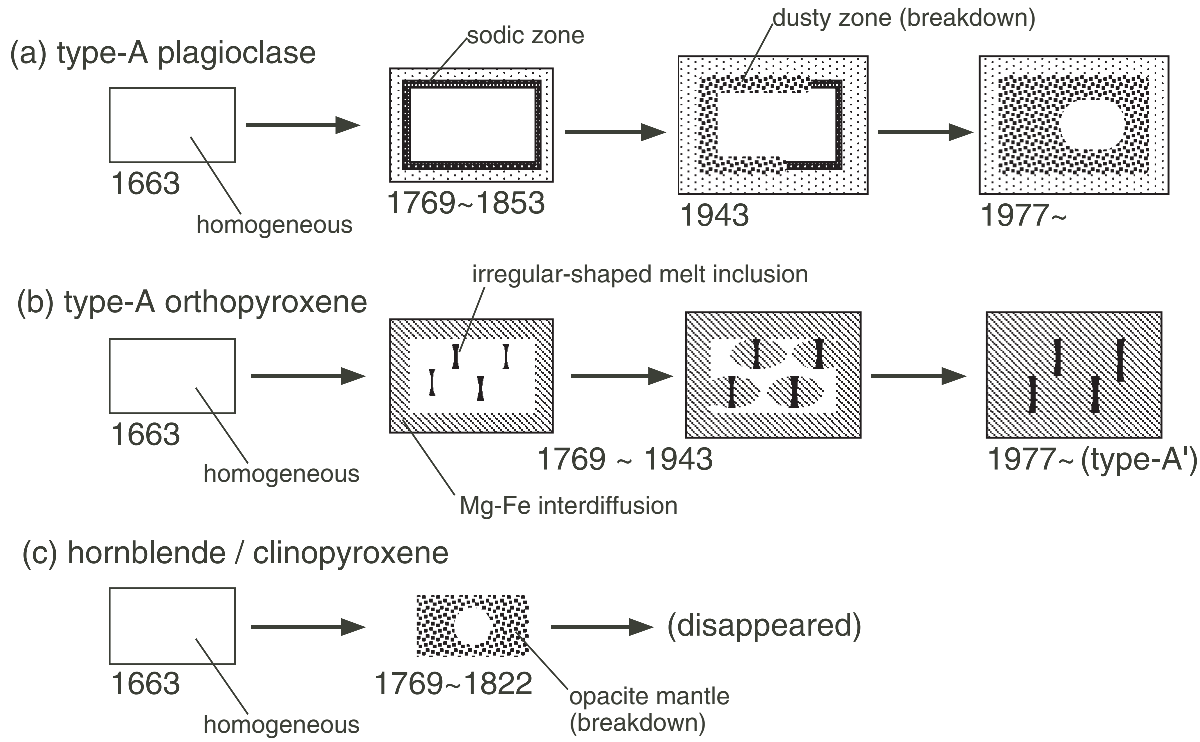

Fig. 15. Schematic sketch of the textural evolution of phenocrysts since 1663. (a) Type-A plagioclase. (b) Type-A orthopyroxene. (c) Hornblende and clinopyroxene.

magma mixing occurred in other eruption episodes is difficult to constrain based on the analysis of pl and opx alone, and hence here we investigate this problem using mt that records the short time scale just prior to eruption.

Discrimination of magma mixing using a magnetite histogram

The compositions of mt (Fig. 12) show sharp peak(s), whereas pl and opx show wide variations in the 1769–1977 products (Figs 3 and 4). The compositional variations of pl and opx represent the integration of all magmatic processes since 1663, but those of mt represent a condition just before eruption because the homogenization time is sufficiently shorter (less than *c.* 10 years) than the time span between the eruptions (*c.* 30–60 years; Table 1). Therefore, each peak in the mt composition histograms corresponds to the condition of the magma that is in equilibrium with the mt just prior to its eruption. If magma mixing took place just prior to the eruption, there should be two or more peaks (groups) in the composition of mt (e.g. Fig. 12a and g).

Two groups of magnetite compositions are obvious for the 1663, 1822, 1853 and 1977 products. On the other hand, it is not obvious whether a second group exists in the 1769 and 2000 products. In the 1769 product, it is possible to recognize a small peak ('peak-II?' in Fig. 12n) with lower Mg/Mn, which is similar to peak-II in 1822 and 1853. Also, in the 2000 product, there is a small peak at Mg/Mn $= 3{\cdot}6$. To support the existence of different magnetite populations, we applied the '*t*-test' to the magnetite groups (Table 5). The split into two peaks (peak-I, peak-II) in the 1663, 1822, 1853 and 1977 products is significant (*t*-ratio $< 0{\cdot}05$) in X_{Usp} and/or Al_2O_3 as well as Mg/Mn. On the other hand, the apparent second peak 'peak-II?' in the 1769 and 2000 products is statistically not significant (*t*-ratio $> 0{\cdot}05$).

Accordingly, in the 1663, 1822, 1853 and 1977 eruptions, two magmas appear to have mixed just before each eruption. Each peak represents the end-member magma mixing in each eruption. In the 1769 and 2000 eruptions, on the other hand, the magnetite provides no evidence of magma mixing (Fig. 12).

There are virtually no type-A and B mt in the products since the 1769 eruption (Fig. 12), in contrast to the observation that type-A and B pl (opx) always exist in the products (Figs 3 and 4). The type-A and B mt phenocrysts were probably dissolved or modified into new peak-I or peak-II types because of rapid diffusion. A few examples with extremely high Al contents (four samples in 1769 and two samples in 1822; Fig. 12h and i) are possibly relicts of type-B mt that have been modified in composition.

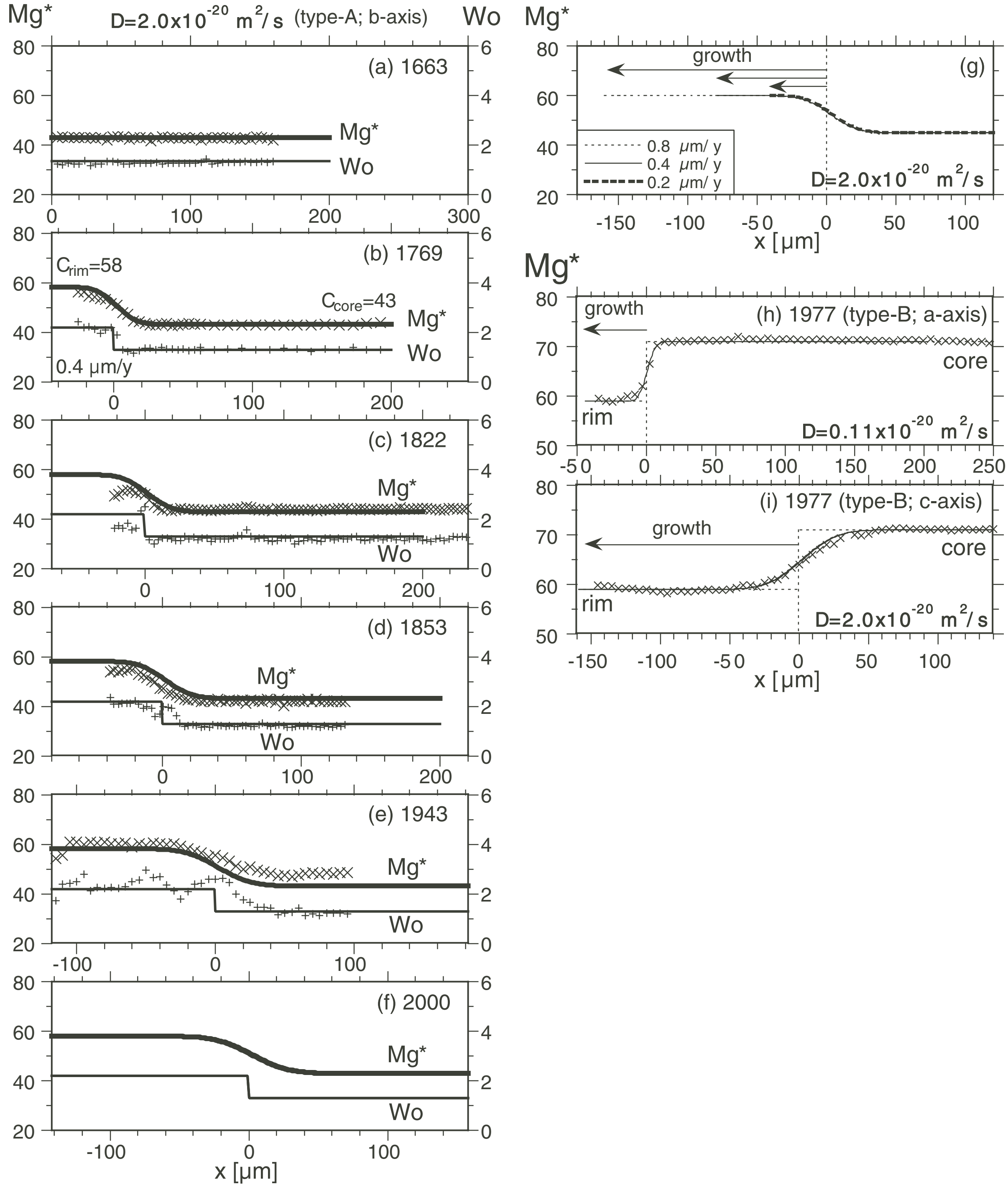

Fig. 16. Calculated zoning profiles of opx by the diffusion-and-growth model (Appendix) compared with actual data. (a)–(f) Results for *b*-axis of type-A opx in the 1663, 1769, 1822, 1853, 1943 and 2000 products (0, 106, 159, 190, 280 and 337 years after 1663, respectively). Bold curve and stepped line are calculated profiles of Mg* and Wo, respectively. Both case 1 (plate) and case 2 (cylinder) are drawn, although they are almost overlap each other. Calculated conditions are as follows: the diffusion coefficient of Fe–Mg interdiffusion D is $2{\cdot}0 \times 10^{-20}$ m^2/s; the diffusion of Wo is neglected; the initial size a of the crystal is 200 μm; the growth rate G is 0·4 μm/year; the initial composition at 1663 is Mg^*_{43} and $Wo_{1{\cdot}3}$; and the rim composition is fixed at Mg^*_{58} and $Wo_{2{\cdot}2}$ since 1663. +, ×, analyzed compositions. The curvature of the profiles is well fitted by the model. (g) Effect of growth rate on the profiles. Other conditions are the same as (d). (h) and (i) Results for *a*-axis (h) and *c*-axis (i) of a type-B opx phenocryst (Fig. 8f) in the 1977 product (314 years after 1663). The *a*-axis profile can be fitted by $D = 0{\cdot}11 \times 10^{-20}$ m^2/s, much smaller than the *b*-axis value, whereas that of the *c*-axis can be fitted by the same value as the *b*-axis ($D = 2{\cdot}0 \times 10^{-20}$ m^2/s). The growth rate is 0·133 μm/year for (h) and 0·48 μm/year for (i).

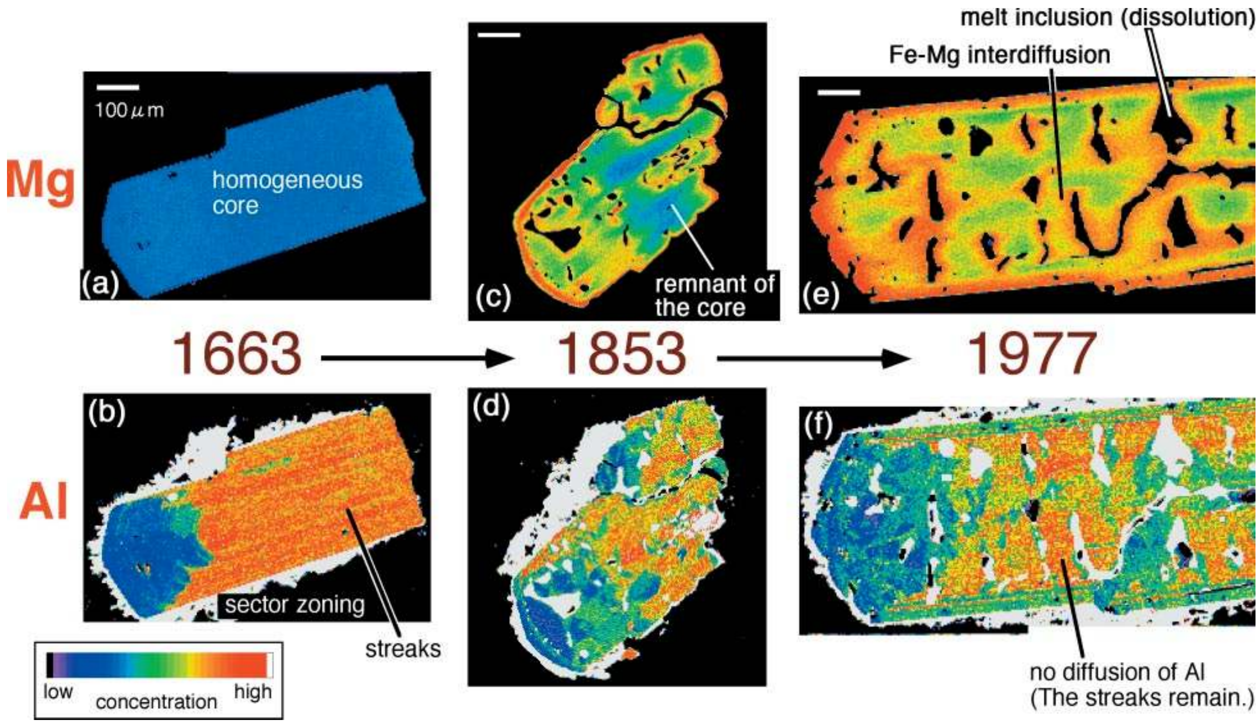

Fig. 17. Element mapping of type-A and type-A′ opx in the 1663 (a, b), 1853 (c, d) and 1977 (e, f) products. The 1663 opx and the 1977 opx are identical to those in Fig. 7a and Fig. 7f, respectively (because of repolishing, Fig. 7f and Fig. 17e and f are slightly different in, for example, the shape of inclusions). The resolution of each image is 4 μm/pixel for (a), (b), (e) and (f), and 3 μm/pixel for (c) and (d). (a, c, e) Mg distribution maps. The initially homogeneous core (Mg^*_{45}; blue) is reduced in the 1853 sample (denoted as 'remnant of the core') and has disappeared in the 1977 sample. The mantle (growth part since 1663) can be seen as a red margin of several tens of microns (c, e). The irregular-shaped melt inclusions (dissolution part) are the black holes within the core. Around them (several tens of microns), a high-Mg region (yellow to red; denoted as 'Fe–Mg interdiffusion') is developing, especially along the *c*-axis (elongated direction). (b, d, f) Al distribution maps. In the 1663 sample, we recognize sector zoning with low Al content (blue) in the *c*-axis direction, and many streaks (yellow in the red region; green in the blue region). These characteristic textures can also be seen in the 1853 and 1977 samples, in spite of significant dissolution. Furthermore, in the high-Mg region around the melt inclusions, there is no change in Al content [denoted as 'no diffusion of Al' in (f)] from 1663 (b). This strongly suggests that the high-Mg region around the melt inclusions is formed by Fe–Mg interdiffusion.

The relationship between peaks (I, II) of mt and types (A, B, C) of pl (and opx) is clear for the 1663 pumice, but not as simple for other samples. To investigate the relationship, phenocryst aggregates (especially pl + mt) were analyzed. In this analysis, we chose aggregates in which the mt is embedded in the margins of pl. Aggregates where mt is completely included or only touches the pl were excluded. If we compare core compositions of pl (An) and mt (Mg/Mn; Fig. 18a and b), their compositional relationship is unclear. This is because the core composition of pl records a magmatic condition that is 'older' than that of mt (just prior to eruption). Thus, we have to compare the 'rim' ($\leq$10 μm from the edge) compositions of pl with the core compositions of mt (Fig. 18c and d). Our analysis reveals that the compositions of pl rims with peak-I mt differ from those with peak-II mt. This suggests that each mt and pl rim pair represents the condition just before eruption. It should be noted that either peak-I or peak-II mt coexists with type-A pl. This means that both magma batches corresponding to peak-I and peak-II mt phenocrysts can originate from the 1663 magma.

Compositions of the end-member magmas

The composition of each end-member magma is estimated as follows (Table 6). The mixing end-members in 1663 have been estimated to be rhyolite (74 wt % SiO_2) and basaltic andesite (54 wt % SiO_2) (Tomiya & Takahashi, 1995). In the case of the 1769 and 2000 pumices, which show no indication of magma mixing, the magma that contains peak-I mt is identical to the eruptive product itself: i.e. a dacite with 72 wt % SiO_2 in 1769 and a dacite with 69 wt % SiO_2 in 2000 (Table 2). The end-member magmas that contain peak-I mt in the 1822 and 1853 pumices and peak-II mt in the 1977 pumices are also dacitic because: (1) their Mg/Mn values are between that of the 1769 dacite and the 2000 dacite (Fig. 12m–r); (2) the temperatures, ranging from 825 to *c.* 900–1000°C (Fig. 14b), are consistent with those of dacite magmas (Cas & Wright, 1987). The

Table 5: Results of t-test for the two groups of magnetite composition

	t-ratio*					
	1663 (I & II)	1769 (I & II?)	1822 (I & II)	1853 (I & II)	1977 (I & II)	2000 (I & II?)
X_{Usp}	<0·0001	0·5849 (n.s.)	0·0026	0·1208 (n.s.)	<0·0001	0·1730 (n.s.)
Al_2O_3 (wt %)	<0·0001	0·6677 (n.s.)	<0·0001	<0·0001	<0·0001	0·4455 (n.s.)
Mg/Mn	<0·0001	<0·0001	<0·0001	<0·0001	<0·0001	<0·0001
Definition of peak-II (or -II?)	Mg/Mn >2	Mg/Mn <1·3	Mg/Mn <1·5	Mg/Mn <1·5	Mg/Mn <3·6 & Al_2O_3 <2·6 wt %	Mg/Mn <3·8

*If *t*-ratio is >0·05 (5%), there is no significance (n.s.) in difference between the two groups.

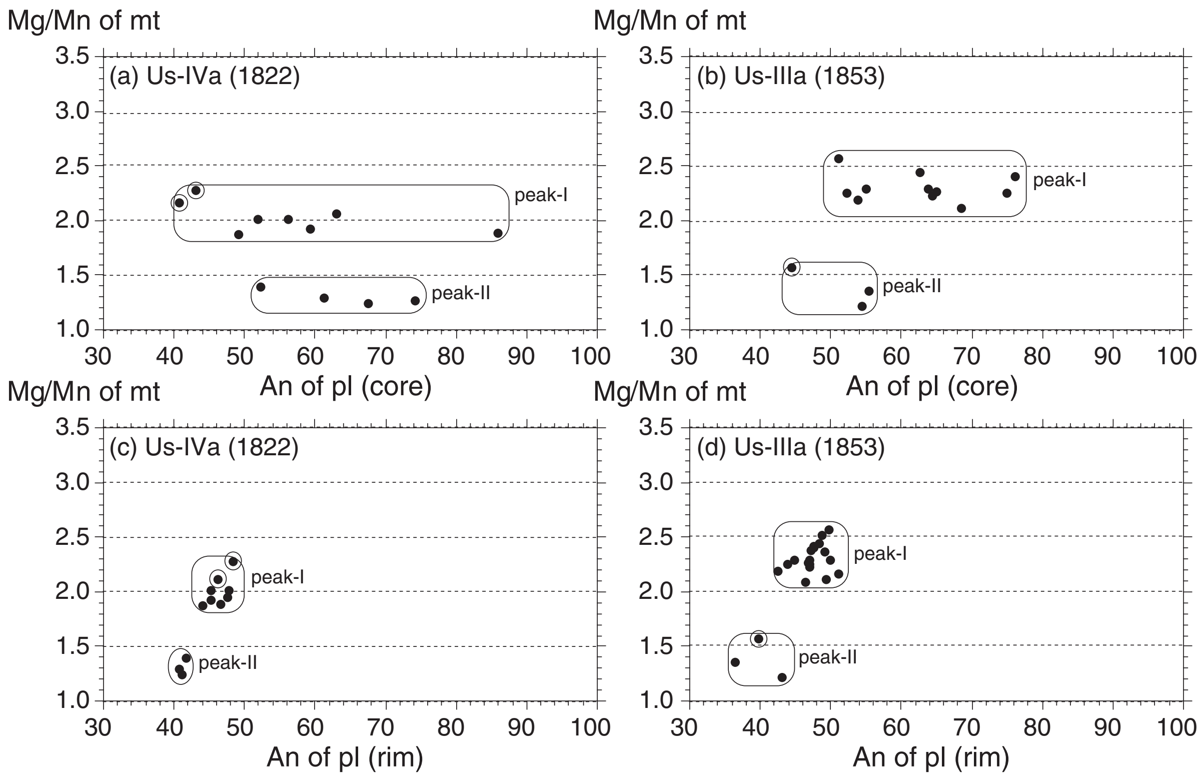

Fig. 18. Compositional relationship between Mg/Mn of mt (peak-I or -II) and An content of pl phenocrysts that are in a contact relationship. Both parameters are sensitive to the temperature of the magma. The relationship between mt and the core of pl is obscure both in Us-IVa (a) and Us-IIIa (b). On the other hand, mt and the rim of pl in both Us-IVa (c) and Us-IIIa (d) show good correlations. It should be noted that type-A pl (circled) coexists with both peak-I and peak-II.

end-member magma that contains peak-I mt in the 1977 pumice is similar to the dacite erupted in 2000; both have the same mt composition (X_{Usp}, Al_2O_3, Mg/Mn). The end-member magma that contains peak-II mt in the 1822 and 1853 pumice is probably rhyolite because of its low temperature (*c.* 750°C), which can be achieved only in a rhyolite magma (Cas & Wright, 1987), and it is more silicic than the bulk composition of the pumice (71 wt % SiO_2).

The combination of mixing end-members in each eruptive product varies with time (Table 6). In 1663, it is rhyolite + basaltic andesite. In 1769, 1822 and 1853, it is dacite ± rhyolite. In 1977 and 2000, it is dacite ± dacite. The three combinations correspond to the three types of rock texture described above. Thus, we conclude that the difference in rock texture is caused by differences between the magma mixing end-members just prior to each eruption.

A new magma batch in 1977?

The mt composition drastically changed between 1853 and 1977 (Fig. 12). The Al contents and Mg/Mn values

Table 6: Estimated end-members of magma mixing in the Usu magma chamber

Age (AD)	peak-I			peak-II		
	Type	SiO_2 (wt %)	T (°C)	Type	SiO_2 (wt %)	T (°C)
1663	Rhyolite	74	780	Basaltic andesite	54	1020
1769	Dacite	72	825	(no mixing?)		
1822	Dacite	~70–71*	830	Rhyolite	≥71	750
1853	Dacite	~70–71*	860	Rhyolite	≥71	750
1977–1978	Dacite†	~69	~950	Dacite‡	~70–71*	~900
2000	Dacite	69	~950	(no mixing?)		

*Should be between 69 and 72.
†A new magma batch?
‡The successor of the peak-I of 1769–1853?

of peak-I and peak-II mt appear to increase. Although there were two eruptions between 1853 and 1977, they were not pumice eruptions, and the change in magnetite compositions during this period is unclear. However, because the petrographic characteristics of the 1943–1945 products are similar to those of the 1769–1853 products [texture (2); Table 2, Fig. 2], we consider that a drastic change in the magma chamber systems occurred between 1945 and 1977.

Since 1977, the end-members of magma mixing changed to 'dacite + dacite' from 'dacite + rhyolite' (Table 6). This suggests that a new dacite evolved prior to 1977. The change of end-member can explain the drastic change in Al contents and Mg/Mn values of mt. In addition, the Al change could be also caused by the change in melt composition as a result of, for example, abundant plagioclase crystallization.

The peak-II mt in 1977 could be the successor of peak-I from 1769 to 1853, because of the similarity of X_{Usp} (Fig. 12); consequently, peak-I in 1977 could be the newcomer. In this case, the magma chamber may have been almost completely replaced during the period 1977–2000 because the 2000 product contains only peak-I. This can explain why type-A and type-B phenocrysts are so rare in the 2000 product (Figs 3 and 4). The new magma batch may rejuvenate the chamber, and this could be the reason why a Plinian-type of eruption resumed in 1977 after an interval of 120 years (Table 1).

Time scale of magma mixing

The period from magma mixing to eruption is short as deduced from the narrow zoning (X_{Usp}) of mt rims (Fig. 13). The zoning width of about 10 μm corresponds to a time of about 3·4 days (at 900°C) to 27 days (at 800°C), using the diffusion coefficient of Ti discussed earlier and the following equation (Jaeger, 1968):

$$L = 1{\cdot}82(Dt)^{1/2}$$

where L is the zoning width, D is the diffusion coefficient and t is the diffusion time. This simple 1-D approximation is applicable because the zoning width is much smaller than the radius of the phenocryst. In this calculation, the zoning at the rim is assumed to be formed by diffusion only. Considering the growth effect, the actual diffusion length becomes shorter, hence the diffusion time could be even shorter. The time scale recorded at the rim of the mt (several days to several tens of days) is similar to the duration of precursory seismicity of Usu volcano (Table 1). If this duration corresponds to that of magma ascent, magma mixing occurred just at the beginning of magma ascent, suggesting that magma mixing triggers the eruption in Usu volcano.

Evolution of the magma-feeding system through time

Two magma chambers beneath Usu volcano

We can estimate magmatic pressure on the basis of the pressure dependence of plagioclase composition, assuming water saturation. Figure 19 demonstrates the estimate based on the pressure dependence compiled by Housh & Luhr (1991). It should be noticed that this is a rough estimation, because we ignore the difference in melt composition between the Housh & Luhr compilation and those studied here. When the plagioclase composition (rim) and temperature of peak-I and peak-II mt are plotted in Fig. 19, they fall into two groups; that is, a high-P group (>200 MPa) and low-P group (<200 MPa).

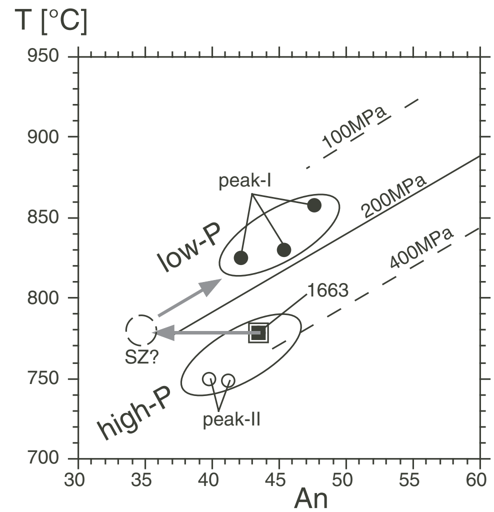

Fig. 19. Estimation of pressure for each magma using the pressure dependence of plagioclase composition. The lines representing pressure are from Housh & Luhr (1991). When we plot the plagioclase composition (rim) and temperature of each magma (from peak-I and peak-II mt–ilm pairs), they can be divided into two groups. The rhyolite in 1663 and the peak-II in 1822 and 1853 are high-*P* group (>200 MPa), whereas peak-I in 1769, 1822 and 1853 are low-*P* group (<200 MPa). The arrows demonstrate a possible path for the peak-I magma after 1663.

The rhyolite in 1663 and the peak-II mt in 1822 and 1853 define the high-*P* group, whereas the peak-I mt in 1769, 1822 and 1853 define the low-*P* group. These two groups probably correspond to two magma chambers—a high-*P* chamber and a low-*P* chamber. Both high-*P* and low-*P* groups contain type-A phenocrysts, as type-A phenocrysts can coexist with either peak-I or peak-II mt (Fig. 18).

Accordingly, we propose the evolution of the magma chamber system beneath Usu volcano as follows (Fig. 20a).

(1) Just prior to the 1663 eruption, there were two homogeneous magmas: a rhyolitic magma with type-A phenocrysts and a basaltic andesite magma with type-B phenocrysts. The two magmas were stratified within a high-*P* (deep) magma chamber (>200 MPa).

(2) The eruptive product of the 1663 eruption was mainly rhyolite. After (or during) the eruption, the two magmas mixed within the magma-feeding system and formed a hybrid dacitic magma (see also Tomiya & Takahashi, 1995, fig. 10). The dacitic magma formed a new shallow magma chamber ($P < 200$ MPa). In the high-*P* magma chamber, on the other hand, part of the rhyolite remained.

(3) Since 1769, the low-*P* chamber and the high-*P* chamber supplied the magma that contained peak-I mt and the one that contained peak-II mt, respectively, at least until 1853. During each eruption (except 1769 and 2000?), mixing of these magmas occurred, which triggered the eruption.

According to the above explanation, the magma in the low-*P* chamber suffered significant decompression after the 1663 eruption (Fig. 20a). This decompression probably caused the formation of the SZ in pl phenocrysts (Fig. 19). After SZ formation, hybridization between the rhyolite and the mafic magma occurred, causing the additional growth of plagioclase mantles with increasing An content outward (Fig. 9).

Temperature increase of magma

The temperature of the magma in the shallow chamber (peak-I) increases with time (Fig. 14b). As mentioned above, this increase is linked to compositional changes (from felsic to mafic), evidenced by the increase in Mg/Mn of mt, An of pl (rim), Mg* of opx (rim) and the decrease in SiO_2 of the bulk-rocks (Figs 3, 4, 12 and 14c).

There can be two possible explanations for the temperature increase (Fig. 20b): (1) heating by injection of hot mafic magma; (2) continuous tapping from a magma chamber with a thermal and chemical gradient, where the magma becomes hotter and more mafic with increasing depth (e.g. Okumura *et al.*, 1981; Oba & Katsui, 1983). For the changes between 1663 and 1769, we believe heating resulted from the injection of hot mafic magma into a magma chamber that was filled with rhyolitic magma (Tomiya & Takahashi, 1995). On the other hand, since 1769, there is virtually no Mg- and Al-rich mt that should be present if a mafic magma had been injected into the chamber (e.g. type-B in 1663); on the contrary, the injecting magmas (represented by peak-II mt) appear to be cooler and more silicic. We thus propose the existence of a zoned magma chamber to explain the temperature increase and compositional change since 1769.

CONCLUSIONS

The Usu magma chamber has existed continuously since 1663. The products of all subsequent magmatic eruptions (1769, 1822, 1853, 1943, 1977, 2000) were supplied from the same magma-feeding system. The Usu magma chamber is thus a natural laboratory with a run duration of over 300 years. Using numerical simulations of diffusion and crystal growth, the observed zoning profiles in orthopyroxene can be fitted assuming reasonable diffusion coefficients for Fe–Mg interdiffusion ($2{\cdot}0 \times 10^{-20}$ m^2/s for *b*- and *c*-axis and $0{\cdot}11 \times 10^{-20}$ m^2/s for *a*-axis at ~850°C).

Magma mixing occurred during or just prior to most of the pumice eruptions (1663, 1822, 1853, 1977) on the basis of the bimodal distributions of magnetite composition. The combination of mixing end-members changes

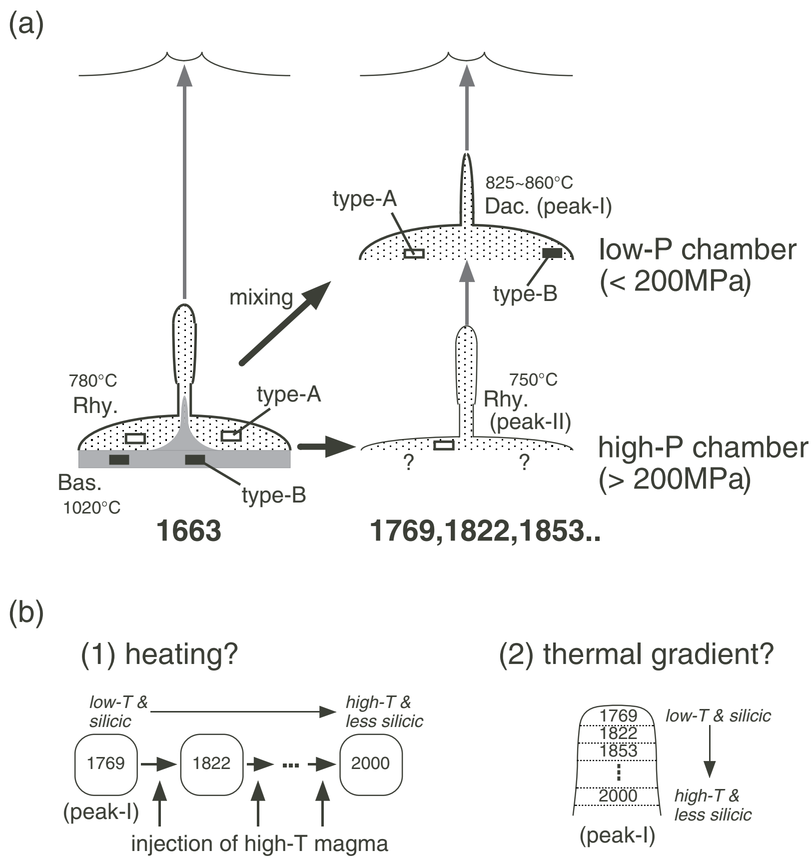

Fig. 20. (a) Evolution of the magma feeding system beneath Usu volcano. Just prior to the 1663 eruption, a rhyolitic magma (Rhy.) with type-A phenocrysts and a basaltic andesite magma (Bas.) with type-B phenocrysts existed (Tomiya & Takahashi, 1995) in a deep magma chamber (>200 MPa). After the eruption, the two magmas mixed and formed a hybrid dacitic magma (Dac.) in a shallow magma chamber (<200 MPa). Part of the rhyolitic magma remained in the deep chamber. Since 1769, the shallow chamber and the deep chamber have supplied the peak-I magma and peak-II magma, respectively. (b) Two models proposed for the temperature increase and compositional change of the peak-I magma since 1769. (1) The temperature increase is caused by heating. The heat is supplied by hot mafic magmas that mix into the chamber. The compositional change is also due to the mixing. (2) The apparent temperature and compositional changes originate from a thermal and chemical gradient within the magma chamber where the lower part is a higher-temperature and more mafic magma. Magmas since 1769 have erupted from the upper part of the chamber in sequence.

with time as follows: rhyolite + basaltic andesite in 1663; dacite ± rhyolite in 1769, 1822 and 1853; dacite ± dacite in 1977 and 2000.

Magnetite is a useful mineral with which to estimate the magmatic conditions just prior to eruption because it always exhibits a homogeneous core equilibrated with the magma, even if other minerals such as plagioclase and orthopyroxene show significant inhomogeneity formed during magma mixing event(s) up to several hundred years earlier. The Mg/Mn value and Al content in magnetite are parameters that are more sensitive to a change in magmatic condition than X_{Usp}, in the case of Usu volcano, and are useful to detect the presence of magma mixing.

In each eruption, the time scale from magma mixing to eruption is less than 10 days, estimated from the width of the zoned rims of magnetite crystals. This time scale is comparable with that of precursory seismicity, suggesting that magma mixing triggers the eruption of Usu volcano.

There are two magma chambers beneath Usu volcano. One is deep (>200 MPa) and the other is shallow (<200 MPa). The former existed prior to the 1663 eruption, whereas the latter probably formed during or just after the 1663 eruption.

The temperature of the magma in the shallow magma chamber increased with time (from 780°C to 900–1000°C). This temperature increase is associated with a change in magma composition, which becomes less silicic, causing dissolution of earlier-formed phenocrysts. The change between 1663 and 1769 can be explained by mixing of a mafic magma injected into a rhyolitic magma in the magma chamber. To explain the temperature increase since the 1769 eruption, the development of a thermal and chemical gradient in the magma chamber is proposed.

ACKNOWLEDGEMENTS

We thank Dr K. Niida (Hokkaido University), who provided important information about sampling sites at Usu volcano. We acknowledge valuable advice from and discussions with Dr Y. Oba (now retired from Yamagata University), Dr T. Koyaguchi (University of Tokyo), Dr I. Miyagi (Geological Survey of Japan; GSJ) and Dr M. Nakamura (now at Tohoku University). Dr Y. Nishimura (Hokkaido University) and Dr T. Yamamoto (GSJ) helped us to survey the 2000 eruptive product. Dr K. Kaneko (now at Kyoto University) provided the programs to process the electron microprobe data. Dr J. Tuff (Cambridge University) read our manuscript and improved it. This paper was greatly improved by valuable comments from Dr D. Geist (the editor), Dr J. W. Cole, Dr D. Morgan and an anonymous reviewer. Professor M. Wilson corrected many grammatical and other errors in the manuscript. This work was partly supported by JSPS Research Fellowships for Young Scientists.

REFERENCES

Bacon, C. R. & Hirschmann, M. M. (1988). Mg/Mn partitioning as a test for equilibrium between coexisting Fe–Ti oxides. *American Mineralogist* **73**, 57–61.

Bowen, N. L. (1913). The melting phenomena of the plagioclase feldspars. *American Journal of Science* **35**, 577–599.

Cas, R. A. F. & Wright, J. V. (1987). *Volcanic Successions Modern and Ancient.* London: Allen & Unwin, 528 pp.

Chou, I.-M. (1987). Oxygen buffer and hydrogen sensor techniques at elevated pressures and temperatures. In: Ulmer, G. C. & Barnes, H. L. (eds) *Hydrothermal Experimental Techniques*. New York: John Wiley, pp. 61–99.

Clynne, M. A. (1999). A complex magma mixing origin for rocks erupted in 1915, Lassen Peak, California. *Journal of Petrology* **40**, 105–132.

Crank, J. (1975). *The Mathematics of Diffusion*, 2nd edn. Oxford: Oxford University Press.

DePaolo, D. J. (1981). Trace element and isotopic effects of combined wallrock assimilation and fractional crystallization. *Earth and Planetary Science Letters* **53**, 189–202.

Feeley, T. C. & Dungan, M. A. (1996). Compositional and dynamic controls on mafic–silicic magma interactions at continental arc volcanoes: evidence from Cordon El Guadal, Tatara–San Pedro Complex, Chile. *Journal of Petrology* **37**, 1547–1577.

Freer, R. & Hauptman, Z. (1978). An experimental study of magnetite–titanomagnetite interdiffusion. *Physics of the Earth and Planetary Interiors* **16**, 223–231.

Ganguly, J. & Tazzoli, V. (1994). Fe^{2+}–Mg interdiffusion in orthopyroxene: retrieval from the data on intracrystalline exchange reaction. *American Mineralogist* **79**, 930–937.

Ghiorso, M. S. & Sack, R. O. (1991). Fe–Ti oxide geothermometry: thermodynamic formulation and the estimation of intensive variables in silicic magmas. *Contributions to Mineralogy and Petrology* **108**, 485–510.

Housh, T. B. & Luhr, J. F. (1991). Plagioclase–melt equilibria in hydrous systems. *American Mineralogist* **76**, 477–492.

Izbekov, P. E., Eichelberger, J. C., Patino, L. C., Vogel, T. A. & Ivanov, B. V. (2002). Calcic cores of plagioclase phenocrysts in andesite from Karymsky volcano: evidence for rapid introduction by basaltic replenishment. *Geology* **30**, 799–802.

Jaeger, J. C. (1968). Cooling and solidification of igneous rocks. In: Hess, H. H. & Poldervaart, A. (eds) *Basalts, Vol. 2*. New York: John Wiley, pp. 503–536.

Katsui, Y., Yokoyama, I., Watanabe, H. & Murozumi, M. (1981). Usu Volcano. In: Katsui, Y. (ed.) *Field Excursion Guide to Usu and Tarumai Volcanoes and Noboribetsu Spa*. Tokyo: Volcanological Society of Japan, pp. 1–37.

Koyaguchi, T. & Kaneko, K. (1999). A two-stage thermal evolution model of magmas in continental crust. *Journal of Petrology* **40**, 241–254.

LaTourrette, T. & Wasserburg, G. J. (1998). Mg diffusion in anorthite: implications for the formation of early solar system planetesimals. *Earth and Planetary Science Letters* **158**, 91–108.

Nakagawa, M. (1998). Usu volcano. In: Takahashi, M. & Kobayashi, T. (eds) *Volcanoes in Hokkaido: Field Guide of Japanese Volcanoes, Vol. 3*. Tokyo: Tsukiji-shokan, pp. 92–113 (in Japanese).

Nakagawa, M., Ishizuka, Y., Yoshimoto, M., Kudo, T., Aizawa, K., Kitagawa, J., Hiraga, N., Matsumoto, A., Togari, H., Takahashi, R., Ishii, E., Egusa, M., Seino, T., Amma-Miyasaka, M., Wada, K. & Niida, K. (2002*a*). Eruptive materials of the 2000 eruption of Usu volcano, Northern Japan: component materials and their temporal change. *Bulletin of Volcanological Society of Japan* **47**, 279–288 (in Japanese with English abstract).

Nakagawa, M., Matsumoto, A., Tajika, J., Hirose, W. & Ohtsu, S. (2002*b*). Re-investigation of eruption history of Usu volcano, Hokkaido, Japan: finding of pre-Meiwa eruption (late 17th century) between Kanbun (1663) and Meiwa (1769) eruptions. *Programme and Abstracts, the Volcanological Society of Japan, No. 2*, 91 (in Japanese).

Nakagawa, M., Wada, K. & Wood, P. (2002*c*). Mixed magmas, mush chambers and eruption triggers: evidence from zoned clinopyroxene phenocrysts in andesitic scoria from the 1995 eruptions of Ruapehu volcano, New Zealand. *Journal of Petrology* **43**, 2279–2303.

Nakamura, M. & Shimakita, S. (1998). Dissolution origin and syn-entrapment compositional change of melt inclusion in plagioclase. *Earth and Planetary Science Letters* **161**, 119–133.

Oba, Y. (1966). Geology and petrology of the Usu volcano, Hokkaido, Japan. *Journal of the Faculty of Science, Hokkaido University, Series IV* **13**, 185–236.

Oba, Y. (1989). Crystal clots from dome lavas (dacite) of Usu volcano, Hokkaido. *Journal of Mineralogy, Petrology and Economic Geology* **84**, 192–199 (in Japanese).

Oba, Y. (1991). Chemical composition of minerals in rocks from Usu volcano, Hokkaido—petrological implications to fractionation of the felsic magma. *Bulletin of the Yamagata University, Natural Science* **12**, 355–376 (in Japanese with English abstract).

Oba, Y. & Katsui, Y. (1983). Petrology of the felsic volcanic rocks from Usu volcano, Hokkaido, Japan. *Journal of Mineralogy, Petrology and Economic Geology* **78**, 123–131 (in Japanese with English abstract).

Oba, Y., Katsui, Y., Kurasawa, H., Ikeda, Y. & Uda, T. (1983). Petrology of historic rhyolite and dacite from Usu volcano, North Japan. *Journal of the Faculty of Science, Hokkaido University, Series IV* **20**, 275–290.

Okumura, Ki., Soya, T., Ono, K. & Satoh, H. (1981). Petrology of rhyolite and dacite erupted in last 300 years from Usu volcano, Japan. *Abstracts 1981 IAVCEI Symposium*, pp. 276–277.

Okumura, Ko. & Sangawa, A. (1984). Age and distribution of Toya pyroclastic flow (abstract). *Bulletin of Volcanological Society of Japan* **29**, 338 (in Japanese).

Oshima, O. (1977). Preliminary report on the mineralogy of the 1977 eruption of Usu volcano (abstract). *Bulletin of Volcanological Society of Japan* **22**, 281 (in Japanese).

Pietruszka, A. J. & Garcia, M. O. (1999). A rapid fluctuation in the mantle source and melting history of Kilauea volcano inferred from the geochemistry of its historical summit lavas (1790–1982). *Journal of Petrology* **40**, 1321–1342.

Sautter, V., Jaoul, O. & Abel, F. (1988). Aluminum diffusion in diopside using the $^{27}Al(p, \gamma)^{28}Si$ nuclear reaction: preliminary results. *Earth and Planetary Science Letters* **89**, 109–114.

Schwandt, C. S., Cygan, R. T. & Westrich, H. R. (1998). Magnesium self-diffusion in orthoenstatite. *Contributions to Mineralogy and Petrology* **130**, 390–396.

Seino, M., Okada, H., Mori, H., Nishimura, Y. & Oshima, H. (2000). Re-examinations of data on the 1910 eruption of Usu volcano. *Programme and Abstracts, the Volcanological Society of Japan, No. 2*, 40 (in Japanese).

Smith, D. & Barron, B. R. (1991). Pyroxene–garnet equilibration during cooling in the mantle. *American Mineralogist* **76**, 1950–1963.

Soya, T., Katsui, Y., Niida, K. & Sakai, K. (1981). *Geological Map of Usu Volcano, 1:25 000.* Tsukuba: Geological Survey of Japan (in Japanese with English abstract).

Stormer, J. C. (1983). The effects of recalculation on estimates of temperature and oxygen fugacity from analyses of multi-component iron–titanium oxides. *American Mineralogist* **68**, 586–594.

Tomiya, A. & Takahashi, E. (1995). Reconstruction of an evolving magma chamber beneath Usu volcano since the 1663 eruption. *Journal of Petrology* **36**, 617–636.

Tomiya, A., Miyagi, I., Hoshizumi, H., Yamamoto, T., Kawanabe, Y. & Satoh, H. (2001). Essential material of the March, 31, 2000 eruption of Usu volcano: implication for the mechanism of the phreatomagmatic eruption. *Bulletin of Geological Survey of Japan* **52**, 215–229 (in Japanese with English abstract).

Tsuchiyama, A. (1985). Dissolution kinetics of plagioclase in the melt of the system diopside–albite–anorthite, and origin of dusty plagioclase in andesites. *Contributions to Mineralogy and Petrology* **89**, 1–16.

Tsuchiyama, A. & Takahashi, E. (1983). Melting kinetics of a plagioclase feldspar. *Contributions to Mineralogy and Petrology* **84**, 345–354.

Umino, S. & Horio, A. (1998). Multistage magma mixing revealed in phenocryst zoning of the Yunokuchi Pumice, Akagi volcano, Japan. *Journal of Petrology* **39**, 101–124.

Zellmer, G. F., Sparks, R. S. J., Hawkesworth, C. J. & Wiedenbeck, M. (2003) Magma emplacement and remobilization timescales beneath Montserrat: insights from Sr and Ba zonation in plagioclase phenocrysts. *Journal of Petrology* **44**, 1413–1431.

APPENDIX: NUMERICAL SIMULATION OF DIFFUSION AND GROWTH IN A CRYSTAL

A model for diffusion and growth in a crystal

To interpret the zoning profiles of opx in the Usu rocks (Fig. 10), we conducted numerical simulations using a model to reproduce both diffusion and growth in a crystal (Fig. A1). For simplicity, the following assumptions were adopted.

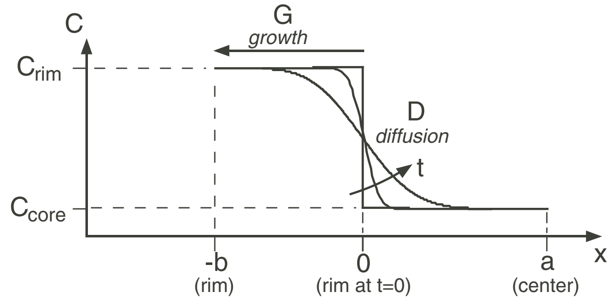

Fig. A1. A model reproducing both diffusion and growth in a crystal. The crystal is initially homogeneous (at $t = 0$, $c = c_{\mathrm{core}}$ for $0 \leq x \leq a$). For $t > 0$, the rim composition is fixed at another value ($c = c_{\mathrm{rim}}$) and the rim position ($x = -b$) moves by crystal growth $b = Gt$, where G is the growth rate. Within the crystal, diffusion occurs controlled by the diffusion coefficient of D.

(1) Diffusion and growth can be treated in one dimension.

(2) Temperature is constant, and the dependence of compositional parameters (such as Mg*) on the diffusion coefficient, D, can be neglected, both of which allow us to assume that the diffusion coefficient is constant.

(3) The initial crystal is homogeneous with a composition of $c = c_{\mathrm{core}}$.

(4) The composition of the additional growth, c_{rim}, is constant, and the growth rate, G, is constant during growth.

We consider the following two cases for crystals of different shapes: case 1, diffusion in a plate; case 2, diffusion in a cylinder. The latter case provides a better simulation of diffusion in orthopyroxene, where diffusion along the a-axis is negligible because it is much slower than that along the b- and c-axis (Ganguly & Tazzoli, 1994).

Thus, we use the equations (e.g. Crank, 1975)

$$\frac{\partial c}{\partial t} = D\frac{\partial^2 c}{\partial x^2} \text{(for case 1)}$$

and

$$\frac{\partial c}{\partial t} = D\frac{1}{r}\frac{\partial}{\partial r}\left(r\frac{\partial c}{\partial r}\right) = D\frac{1}{a-x}\frac{\partial}{\partial x}\left[(a-x)\frac{\partial c}{\partial x}\right] \text{(for case 2)}$$

for $-b \leq x \leq a$, where t is time, x is distance from the initial rim, r is distance from the center ($= a - x$), b is the mantle width, and a is the half-width (case 1) or radius (case 2) of the crystal. The mantle width is given by

$$b = Gt.$$

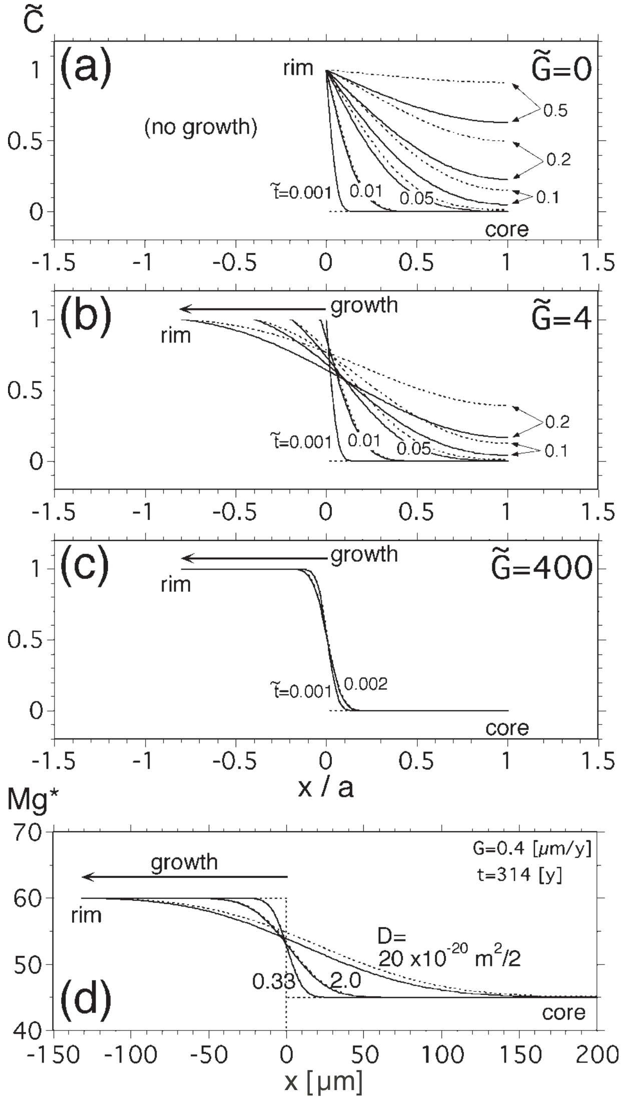

Fig. A2. Results of the numerical simulation. Continuous lines and dotted lines are the results for a plate and a cylinder, respectively. (a)–(c) Results of non-dimensional calculation. Vertical axis is non-dimensional concentration $\tilde{c}$, and horizontal axis is non-dimensional position $\tilde{x} = x/a$. As the non-dimensional growth rate $\tilde{G}$ increases, the relative effect of growth with respect to diffusion increases. (d) Calculation showing the effect of D. Parameters used are $a = 200\,\mu$m, $G = 0{\cdot}4\,\mu$m/year and $t = 314$ years ($b = 125{\cdot}6\,\mu$m), for opx in the 1977 product. In this calculation, $\tilde{G}$ is 12·7, 127 and 761 when D is 20, 2·0 and $0{\cdot}33 \times 10^{-20}$ m^2/s, respectively.

At $x = a$, a symmetrical boundary condition is adopted (i.e. $\partial c/\partial x = 0$).

In the calculation, we used the following non-dimensionalization:

$$\tilde{c} = \frac{c - c_{\mathrm{core}}}{c_{\mathrm{rim}} - c_{\mathrm{core}}}, \tilde{x} = \frac{x}{a}, \tilde{b} = \frac{b}{a}, \tilde{t} = \frac{Dt}{a^2} \text{ and } \tilde{G} = \frac{Ga}{D},$$

yielding

$$\frac{\partial \tilde{c}}{\partial \tilde{t}} = \frac{\partial^2 \tilde{c}}{\partial \tilde{x}^2} \text{(case 1)}$$

$$\frac{\partial \tilde{c}}{\partial \tilde{t}} = \frac{1}{1 - \tilde{x}} \frac{\partial}{\partial \tilde{x}} \left[(1 - \tilde{x}) \frac{\partial \tilde{c}}{\partial \tilde{x}} \right] \text{ (case 2)}$$

and $\tilde{b} = \tilde{G}\tilde{t}$, for $-\tilde{b} \leq \tilde{x} < 1$. $\tilde{G}$ is the parameter showing the relative effect of G (growth) and D (diffusion).

The above equations were solved numerically by an explicit finite difference method.

Results of numerical simulation

Results of the model numerical simulation are shown in Fig. A2. As the non-dimensional growth rate $\tilde{G}$ increases, the relative effect of growth with respect to diffusion increases. If $\tilde{G} = 0$ (Fig. A2a), there is no growth, reflecting simple diffusion at a fixed boundary condition; this agrees with the well-known results of, for example, fig. 4.1 (for case 1) or fig. 5.3 (for case 2) of Crank (1975). The results of case 1 and case 2 are similar when $\tilde{t} < 0{\cdot}05$, but separate out for $\tilde{t} > 0{\cdot}1$. In both cases, the composition of the center ($\tilde{x} = 1$) departs from the initial value ($\tilde{c} = 0$) when $\tilde{t}$ exceeds $\sim 0{\cdot}05$. If $\tilde{G}$ is of the order of unity (Fig. A2b), growth and diffusion effects are comparable. If $\tilde{G}$ is $\gg 1$ (Fig. A2c), growth is dominant, or, in other words, diffusion is becoming negligible. If $\tilde{G} = \infty$ (not shown), no diffusion occurs.

Figure A2d shows the effect of D at $G = 0{\cdot}4\,\mu$m/year and $t = 314$ years, for opx in the 1977 product. The core composition remains at the initial value (Mg*$_{45}$) even with a high D value (e.g. 20×10^{-20} m^2/s) if the crystal size is 200 μm or larger.